Heliyon 9 (2023) e17363

Contents lists available at ScienceDirect

Heliyon

journal homepage: www.cell.com/heliyon

Lithological discrimination and mineralogical mapping using Landsat-8 OLI and ASTER remote sensing data: Igoudrane region, jbel saghro, Anti Atlas, Morocco

Soukaina Baid *, Abdelhalim Tabit, Ahmed Algouti, Abdellah Algouti, Imane Nafouri, Sabir Souddi, Abdelfattah Aboulfaraj, Salma Ezzahzi, Akram Elghouat

Department of Geology, Geoscience Geotourism Natural Hazards and Remote Sensing Laboratory (2GRNT), Faculty of Sciences Semlalia, University of Cadi Ayyad, BP 2390, 40000 Marrakesh, Morocco

ARTICLE INFO

Keywords:
Lithological discrimination
Mineralogical mapping
Alteration
BR
PCA
MNF
ICA
XRD
Reflectance spectrometry

ABSTRACT

This study aims to delineate the lithological formations, in addition to a mineralogical mapping comparing between the ASTER and Landsat-8 OLI sensors in the Igoudrane region. The research was accomplished using BR along with spectral profiles of minerals, PCA, MNF, ICA, XRD, and reflectance spectrometry. The BR measured with ASTER revealed the presence of amphibole, illite, smectite, muscovite, phengite, basic degree index SiO2, calcite, chlorite, epidote, dolomite, hydroxides, and ferrous silicates. Furthermore, Landsat-8 OLI BR highlighted areas with oxides, hydroxides, and laterite. The spectral profiles of minerals showed their absorption in the VNIR and SWIR regions. The muscovite and illite (phyllic alteration) are distinguished by Al–OH absorption at 2.20 μm. The argillitic alteration is additionally defined by muscovite, illite, and Kaolinite, where Kaolinite has a high absorption at 0.9 μm. Chlorite and carbonates characterized the propylitic alteration zone, with an absorption ranging between 2.3 μm and 2.35 μm due to CO3 and Mg–OH compositions. The oxidation (hematite and jarosite) was distinguished by absorption near 0.95 μm and 2.3 μm, respectively, whereas the goethite spectral profile exhibits absorption near 1.4 μm and 2.2 μm. The absorption of smectite is 1.4 μm, near 2.2 μm. The amphibole had absorption near 1.4 μm and 2.3 μm, whereas the pyroxene had absorption near 1.4 μm and 2.3 μm. The first three components of PCA, MNF, and ICA showed the highest eigenvalues and gave an appreciable discrimination of the lithologies, especially with ASTER. Moreover, the XRD quantified the mineralogy of the rocks, which were compared to the BR of ASTER. The reflectance spectrometry also provided alteration minerals, such as muscovite, phengite, illite, Fe–Mg chlorite, Fe-chlorite, iron oxides, hydroxides, hornblende, and calcite. Overall, the methodology adopted has shown great performance and strong potential for mapping alteration areas and lithological discrimination in similar arid regions.

* Corresponding author.
E-mail addresses: baidsoukaina97@gmail.com, soukaina.baid@ced.uca.ma (S. Baid).

https://doi.org/10.1016/j.heliyon.2023.e17363
Received 2 January 2023; Received in revised form 12 June 2023; Accepted 14 June 2023
Available online 21 June 2023

1. Introduction

Recently, mineralogical mapping and lithological discrimination have both benefited from remote sensing [1–4]. The ASTER and Landsat-8 OLI were used in this study in the purpose that they had proven their efficiency in lithological discrimination, mineralogical mapping, also in detecting the altered zones [5]. The multispectral bands of ASTER launched on December 1999 were used in order to extort geological information for mineralogical and alteration mineral mapping [6,7] (lpdaac.usgs.gov/products/ast_l1tv003/). It may also be used for extracting lineaments automatically using the conventional methods such as the LINE algorithm of Geomatica software [8]. Moreover, ASTER makes available a GDEM elevation data [9,10]. Landsat-8 OLI launched on February 11th, 2013, has nine spectral bands with a spatial resolution of 30 m (bands 1 to 7, 9), and a panchromatic band (15 *m*). The data was gathered from the NASA-USGS (United States Geological Survey), with UTM projection coordinate system, zone 30 north (ASTER), and zone 29 north (Landsat-8 OLI), WGS84 as its datum (usgs.gov/Landsat-missions/Landsat-8).

The NIR, SWIR, as well as the VNIR spectral responses are influenced by chemical and mineralogical constitution of the rocks [11, 12]. The visible and VNIR bands are primarily responsive to metal oxides [10,11,13], while the SWIR one exhibits mineral captivation [10,14,15], and has proven its good contribution on lithological studies [16,17]. The TIR offers emissivity data, allowing mapping of carbonates and sulfides [18–20], and it's important especially for the discrimination of silicate minerals [21].

Several studies highlighted the utility of ASTER and Landsat sources in lithological discrimination. Gad and Kusky (2007) suggested an updated BR for ASTER data (4/7, 4/6, and 4/10) for identifying both metamorphic and igneous rocks in dry locations. Amer et al. (2010) created for the first-time BR using ASTER images to cartography serpentinites in arid zones [(2 + 4)/3, (5 + 7)/6, and (7 + 9)/8], as well as identifying the ophiolitic and granitic rocks using RGB composite [11]. Leverington and Moon (2012) mapped the igneous and metamorphic rocks using Landsat TM data, applying a linear unmixing technique, ground reflectance, and a neural network classifier. The results he obtained demonstrated the unmixing method's inferiority in mapping geological features when compared to the neural network classifier [1]. Eldosouky (2021) employed ASTER data to distinguish the facies that are able to host metals. Thus, aeromagnetic data was used to outline the different fractures as well as how they are associated with mineral deposits in three dimensions [22]. New researches have employed and highlighted the efficiency of ASTER images for lithological discrimination [23–26].

Other authors showed the utility of ASTER and Landsat-8 OLI in mineralogical and alteration mapping. Zhang (2016) mapped hydrothermal alteration among Urumieh Dokhar's strongest potential regions. By using ASTER and OLI sensors, they applied several remote sensing processing techniques such as BR, RGB composites, and PCA. All altered zones were effectively identified based on the spectral signature of all types of alteration minerals, such as argillic, prophylitic, and phyllic ones. The findings illustrate the utility of the Landsat-8 OLI sensor in alteration mapping [5]. Moradi (2017) used Landsat imagery of the Lar region in the south of Iran in order to improve the importance of hydrothermal alteration areas in mineral exploration. The study includes RGB composites, BR, and filters. The results showed the relationship between lineament features and alteration, along with mineral presence in the region, allowing them to discover the Cu–Mo porphyry system [27]. Osinowo (2021) used BR and single band combination, which represent the combination of three distinct spectral bands into a single one that can highlight the different geological structures, to identify mineral alteration regions in the Pala Maya Kebbi region (SW of Chad). Their results were bolstered by hydrothermal rocks associated with gold mineralization [28].

Furthermore, other authors used ASTER and Landsat-8 OLI in the Anti Atlas of Morocco for lithological discrimination, alteration and mineralogical mapping. Massironi (2008) ASTER images to map the Precambrian basement of Saghro massif, eastern Anti Atlas, in order to discriminate the lithological units and mineralized fractures. They applied BR, PCA and RGB composites on the VNIR and the SWIR bands, which were selected and interpreted based on the field investigation and the petrographic study. Moreover, the TIR and VNIR/SWIR identified the granitoids plutons. The SAM and MLL were also executed on VNIR/SWIR data to evaluate their potential for discriminating granitoid rocks [29]. El Janati (2014) mapped the Precambrian basement of the Iguerda inlier in the Central Anti-Atlas using ASTER. MNF, Purity pixel index and endmember extraction, spectral angle mapper (SAM), spectral information divergence (SID), and maximum likelihood (MLC) classifications were applied [30]. Adiri (2016) compared the potentialities of ASTER and Landsat-8 OLI images in lithological discrimination in Bas Drâa inlier, Anti Atlas. They used PCA, BR, and support vector machine (SVM) classification as processing methods [10]. El Janati (2019) used ASTER to identify alteration areas in the Taghdout region of the Anti-Atlas bearing Cu, Au, and Ag mineralization. They also defined the Neoproterozoic rocks, such as the volcano-sedimentary formations and the ophiolitic suites of the ophiolitic Complex (Ouarzazate Group). The methodology followed was based on the PCA, BR and filtering method [31]. Jellouli (2019) employed Landsat-8 OLI data to enhance lithological units in the Kerdous inlier, Anti Atlas. They adopted the PCA, decorrelation stretching (DS), BR, and optimal index factor (OIF) approaches [32]. Adiri (2020) evaluated the capability of Landsat-8 OLI, Sentinel-2A and ASTER data in mineralogical mapping in Sidi Flah-Bouskour inlier, Moroccan Anti-Atlas. The BR, ICA, and mixture tuned matched filtering (MTMF) techniques were used in this study, as well as field investigation for validation of the results [33]. Ouhoussa (2022) utilized Landsat-8 OLI to examine the spectral characteristics of the lithological units in the Oumjrane-Boukerzia Mining District, eastern Anti-Atlas, then identify the alteration areas that might hold significant base metal deposits. They adopted color combinations (RGB), BR, PCA and directionals filters for lineaments extraction [34]. Marzouki (2023) employed Landsat-8 OLI and ASTER images for lithological discrimination and lineaments extraction in the Tiwit region, Jbel Saghro, eastern Anti-Atlas. Several processing techniques was applied, included PCA, MNF, ICA and false color composites [35]. Ouhoussa (2023) Identified hydrothermal alteration areas at the Oumjrane Boukerzia, mining District, Anti Atlas, and this was accomplished by using RGB composites, PCA and BR [36].

The current study's main goal consists on comparing between the potentialities of ASTER and Landsat-8 OLI multispectral sensors, using several processing methods to distinguish between the different geological boundaries, as well as the mineralogical

characteristics of the Igoudrane region, Imiter inlier, Jbel Saghro, Moroccan Anti Atlas. The novelty of the present work highlights the integration of ASTER and Landsat-8 OLI remote sensing techniques in discriminating the lithological units in the Igoudrane region, as well as the mineralogical characteristics of the study area. Moreover, an updated geochemistry was applied, and alteration minerals were identified by reflectance spectrometry, which has never been done in this area; thus, remote sensing approved the results.

2. Geographical location and geological framework of the study area

The Anti Atlas is the major structural domain in Moroccan's southern region [37,38] in which Igoudrane belongs to the eastern Anti Atlas (Jbel Saghro), including Precambrian inliers [39] such as Imiter one where the present work is done (Table 1). The Igoudrane pluton outcrops at the base of the high volcanic massif of the same name, to the east of the Imiter mine, and on the Imiter's inlier NE borderline with a general *E*-W orientation over an area of 5–6 km^2. It is limited to the North by the Paleozoic cliffs, to the east and west by upper Neoproterozoic (NP3, PIII) pyroclastic and volcanoclastic sedimentary rocks that cover it in disagreement, moreover contributing to the detrital contribution the basic conglomerate. In the south it is intrusive in the middle Neoproterozoic (NP2, PII) surrounding metasediments previously described. The massif is composed of three facies, the most developed are located in the core and correspond to granodiorites and tonalites. The third facies observed on the southern border of the massif, and it is very dark, grainy with a dioritic to gabbroic nature. The metasediments and granitoids of the Middle Neoproterozoic NP2 basement have been inter-bedded among the Ediacaran (NP3), that is characterized by powerful volcanic and volcanoclastic suites (Ouarzazate Group). Thus, we note also the volcanic and pyroclastic sequences. The NP3 isn't folded or metamorphized, it begins with a basic conglomerate in very discontinuous pockets. It outcrops at the Ouarzazate's Group bottom, east of the Imiter's mine and elsewhere, where it marks the main tectonic unconformity recognized in the basements of Jbel Saghro [40] [Fig. 1 (a, b), Fig. 2].

3. Methodology and materials

3.1. Data preprocessing

The SWIR bands of ASTER were stacked and resampled to 15 *m* using the nearest neighbor algorithm to keep the original pixel counts in the resampled images [41], before being coupled into the VNIR-SWIR bands, and the TIR bands (90 *m*). The TIR bands were used for band ratios without any atmospheric enhancement, in order to avoid any impact on the raw data [42]. An atmospheric correction using the IAR Reflectance was applied to the VNIR-SWIR bands, with also a radiometric correction adopting the Dark Object

Table 1
Coordinates of the four corners of the study area.

Projection: Transverse Mercator/Units: Degree minutes seconds (DMS)			
Points	X	Y	Elevation range
1	6°01′45,55″ W	31°27′08,33″ N	Z max = 2547 *m*
2	5°16′25,39″ W	31°27′08,33″ N	Z min = 1184 *m*
3	5°16′25,39″ W	31°09′56,68″ N	
4	6°01′45,55″ W	31°09′56,68″ N	

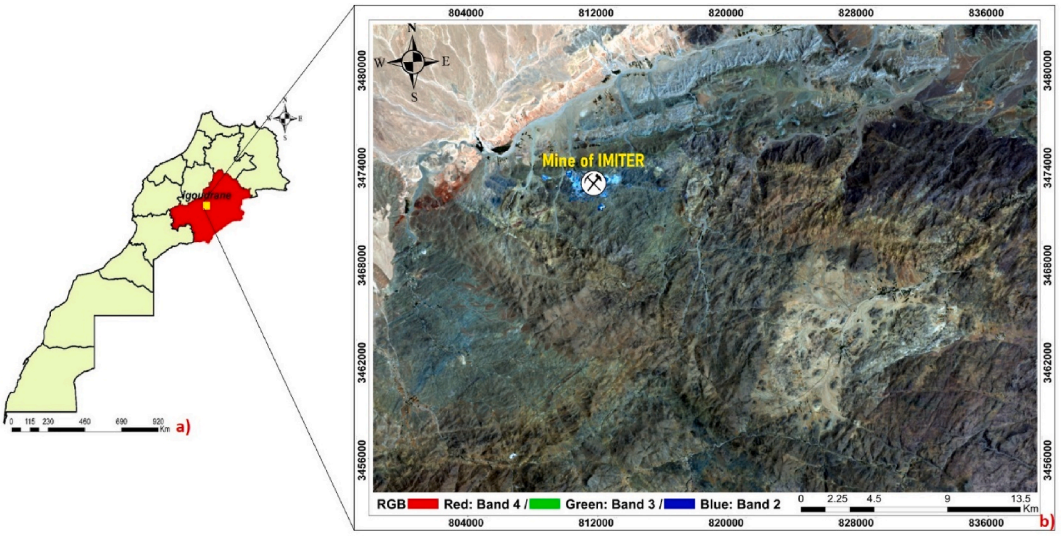

Fig. 1. a) Geographic location of the Igoudrane region, b) RGB visualization of the study area (Landsat-8 OLI).

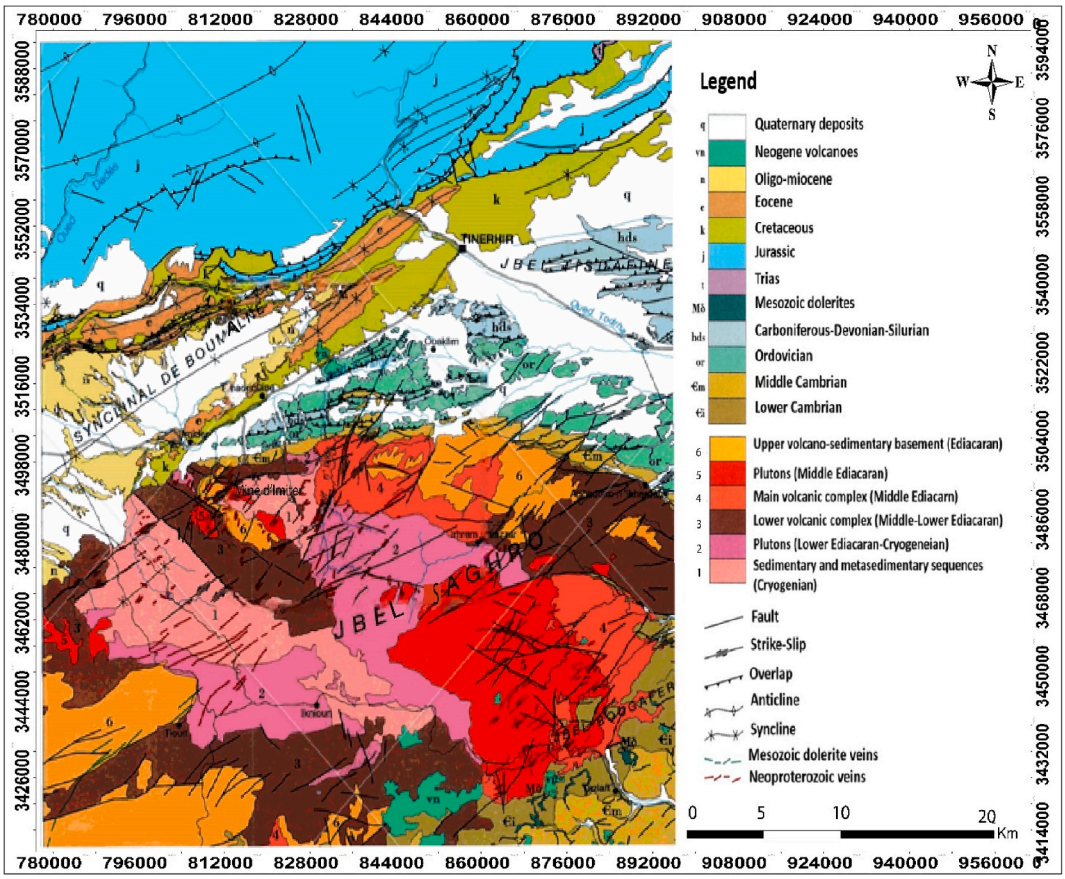

Fig. 2. Simplified geological and structural map of the eastern Anti Atlas 1/500 000.

Subtraction (DOS) [43]**.** Subsequently the atmospheric correction offers the reflectance imagery in which a visual examination of the minerals spectral profiles revealed significant enhancement. Same for Landsat-8 OLI, we applied IAR reflectance.

After preprocessing of Landsat-8 OLI and ASTER images, image noise reduction, RGB combinations, band ratios, PCA, MNF, ICA Transform were applied with classification of the band ratios. ENVI 5.3 and Arc-GIS 10.8 software packages were used to handle the ASTER and Landsat-8 OLI images and prepare GIS layers. The validation of the results of both of the sensors were done using X-Ray diffraction and reflectance spectrometry. The figure below depicts a detailed chart of the methodological approach adopted in this work (Fig. 3).

3.2. Data processing

3.2.1. Band ratio (BR)

BR is a useful technique in remote sensing [13,44]. It requires dividing one band by another one to boost specified items and proprieties which can not be identified in a single band, depending mostly on the concentration of the following minerals: amphibole, carbonate, chlorite, epidote, SiO2, dolomite, ferrous silicates, muscovite, phengite, sericite, illite and smectite with ASTER, as well as iron oxides, ferric oxides, hydroxides and ferrous iron which were highlighted by Landsat-8 OLI band ratios [31,36]. The spectral profiles of alteration minerals were extracted from the IGCP spectral library of ENVI [45], then resampled to ASTER and Landsat-8 OLI images, showing the absorption of minerals in the VNIR and SWIR regions. Sericite alteration generates phyllosilicate minerals, particularly muscovite and illite, which define the phyllic alteration area [46], and are characterized by an absorption of Al–OH at 2.20 μm. The muscovite, illite, and Kaolinite also define the argillitic alteration [33], where the Kaolinite showed a high absorption at 0.9 μm. The propylitic alteration zone is primarily composed of chlorite and carbonates (particularly calcite, dolomite, and epidote). This zone is recognized by a distinctive absorption range of 2.3 μm–2.35 μm caused by CO3 and Mg–OH compositions [47]. The oxidation type of alteration (hematite, jarosite) was characterized by an absorption near 0.95 μm and 2.3 μm, while the goethite spectral profile shows an absorption near 1.4 μm and 2.2 μm. The smectite has an absorption at 1.4 μm and near 2.2 μm. The amphibole gave an absorption at 1.4 μm and 2.3 μm, although the pyroxene was characterized by an absorption near 1.4 μm and 2.3 μm [Fig. 4 (a-d)].

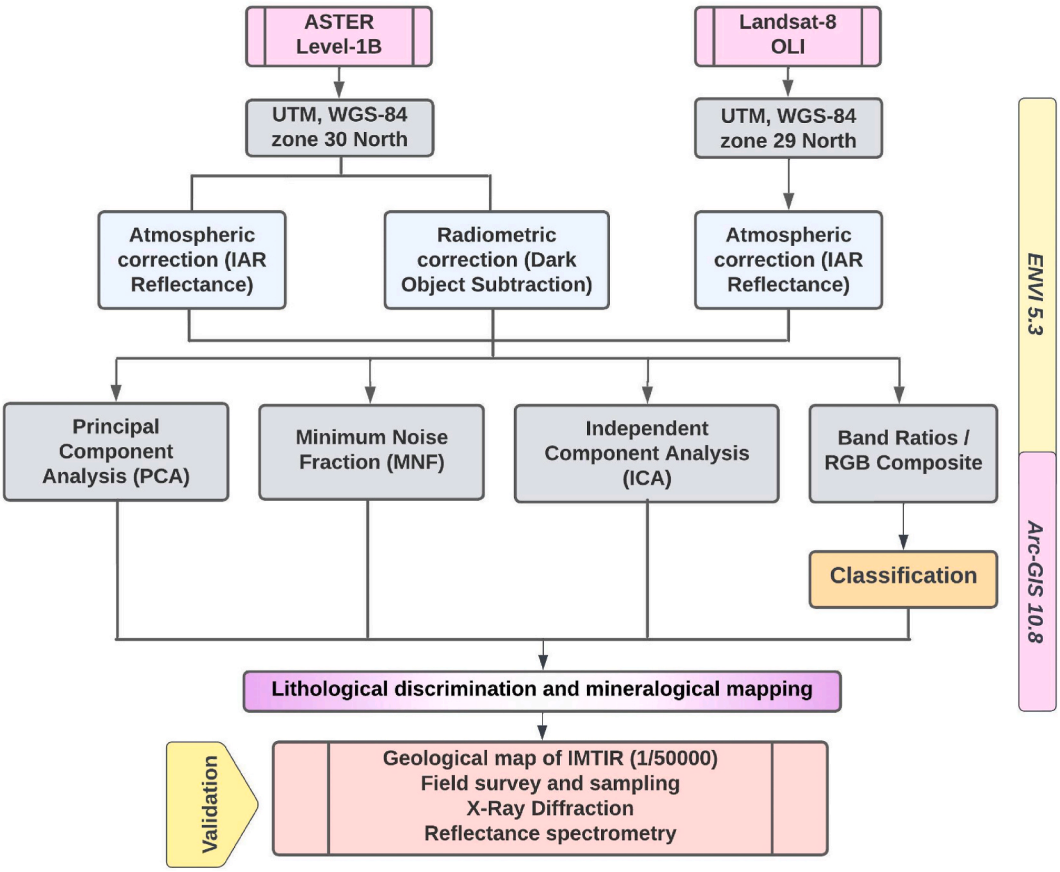

Fig. 3. Methodology chart.

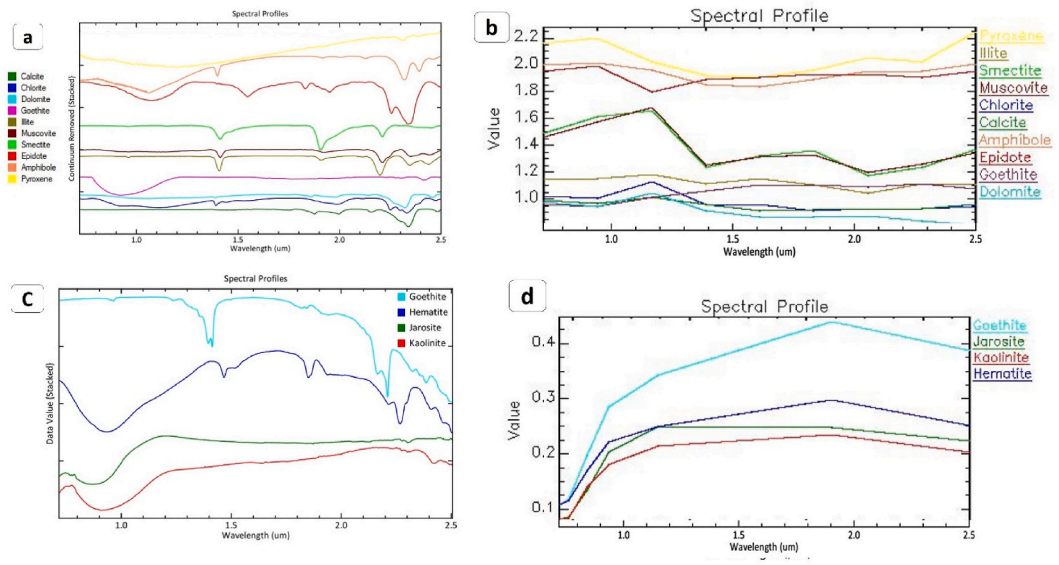

Fig. 4. Spectra of targeted minerals: (a, c) extracted from IGCP library and resampled to ASTER (b), (d) Landsat-8 OLI.

Table 2
Eigenvectors of the PCA bands of ASTER.

Eigenvectors	Band 1	Band 2	Band 3	Band 4	Band 5	Band 6	Band 7	Band 8	Band 9
PC1	0.235	0.298	0.332	0.441	0.377	0.359	0.365	0.296	0.243
PC2	0.271	0.361	0.443	−0.01	0.084	0.122	0.618	0.405	0.18
PC3	0.248	0.31	0.388	−0.107	0.429	0.629	0.277	0.154	−0.033
PC4	−0.111	0.159	0.078	−0.651	0.041	0.418	0.256	0.087	−0.08
PC5	0.041	0.056	0.085	−0.187	0.028	−0.035	−0.542	0.005	0.617
PC6	0.366	0.208	−0.44	−0.133	0.638	−0.443	−0.025	−0.053	−0.074
PC7	0.362	0.408	−0.572	−0.197	−0.5	−0.29	0.008	−0.03	−0.053
PC8	0.115	−0.092	−0.013	−0.077	−0.04	0.001	0.204	−0.567	−0.709
PC9	−0.56	−0.603	−0.097	−0.016	0.078	−0.07	0.041	−0.105	−0.095

Table 3
Eigenvalues and variance of PCA, MNF and ICA (ASTER sensor).

ASTER								
PCA	Eigenvalues %	Variance %	MNF	Eigenvalues %	Variance %	ICA	Eigenvalues %	Variance %
PC1	0.6237	93.47	**MNF1**	0.8733	77.15	**IC1**	0.61	91.41
PC2	0.0324	4.86	**MNF2**	0.1132	10.00	**IC2**	0.0424	6.35
PC3	0.0049	0.73	**MNF3**	0.0761	6.72	**IC3**	0.0086	1.29
PC4	0.0026	0.39	**MNF4**	0.0457	4.04	**IC4**	0.0024	0.36
PC5	0.0016	0.24	**MNF5**	0.0094	0.83	**IC5**	0.0018	0.27
PC6	0.0009	0.13	**MNF6**	0.0061	0.54	**IC6**	0.0007	0.1
PC7	0.0005	0.07	**MNF7**	0.0032	0.28	**IC7**	0.0006	0.09
PC8	0.0004	0.06	**MNF8**	0.0029	0.26	**IC8**	0.0005	0.07
PC9	0.0003	0.04	**MNF9**	0.0021	0.19	**IC9**	0.0003	0.04

Table 4
Eigenvalues and variance of PCA, MNF and ICA (Landsat-8 OLI sensor).

Landsat-8 OLI								
PCA	Eigenvalues	Variance %	MNF	Eigenvalues %	Variance %	ICA	Eigenvalues %	Variance %
PC1	0.2056	93.58	**MNF1**	0.9733	62.80	**IC1**	0.51	82.68
PC2	0.0071	3.23	**MNF2**	0.1902	12.27	**IC2**	0.0924	14.98
PC3	0.006	2.73	**MNF3**	0.1461	9.43	**IC3**	0.0086	1.39
PC4	0.0004	0.18	**MNF4**	0.0657	4.24	**IC4**	0.0024	0.39
PC5	0.0003	0.14	**MNF5**	0.0794	5.12	**IC5**	0.0021	0.34
PC6	0.0002	0.09	**MNF6**	0.0631	4.07	**IC6**	0.0007	0.11
PC7	0.0001	0.05	**MNF7**	0.032	2.06	**IC7**	0.0006	0.10

3.2.2. Principal component analysis (PCA)

PCA has many applications including mineralogical and lithological enhancement [44,48], in which the information within the input images will be compressed into fewer bands known as principal components (PCs) [49]. It eliminates duplicated data, confine PCs noise, then outlines the specific information contained inside the image, which makes minerals and rocks easily recognized [44]**.** The PCA was applied to the SWIR-VNIR bands, and the PCA1, PCA2, PCA3 having the highest eigenvectors and eigenvalues [50] (Tables 2–4).

3.2.3. Minimum noise fraction (MNF)

The MNF was designed to estimate image size, remove noise, and reduce computing time [5,51]. The MNF may be used to transform reflected data, which assists in determining the inherent dimension of the data and distinct the signal noise of it [52]. This approach is frequently used with hyperspectral images since it significantly decreases noise in the raw data [35], then we applied the inverse MNF transformation. The resulted components provide accurate lithological discrimination and hydrothermal alteration detection [53,54]. The first three components involve the maximum of geological information and provide the highest variance (Tables 3 and 4), this is why MNF1, MNF2 and MNF3 were visualized as RGB composite in attempt to differentiate the lithological limits [50,55].

3.2.4. Independent component analysis (ICA)

The ICA has so far been related to data independence. It has a procedure that rotates the input data inside an n-space until they are as independent as possible [56]**.** It is a transformation process that attempts to make the output as independent as possible [33,57]. The first ICA has a high variance, the second has a second high variance, and the last has a low variance, high correlation, and noise, that's why we applied the ICA1, ICA2 and ICA3 as an RGB image (Tables 3 and 4) [58,59]. The ICA showed an appreciable result in

Table 5
BR of ASTER sensor.

Mineral	Band Ratios	References
Amphibole	band 6/band8	[66–68]
Sericite-illite-smectite	(band5+band7)/band6	[69]
Muscovite	band7/band6	[70]
Phengite	Band5/band6	[70]
Basic degree index SiO2	Band12/band13	[36,71]
Carbonate-chlorite-epidote	(band7+band9)/band8	[69]
Dolomite	(band6+band8)/band7	[72]
Simple Ratio MIR Red Eisenhydroxid index	Band6/band2	[73]
Ferrous silicates	Band5/band4	[69]

discriminating the lithological units, when compared to PCA and MNF, it may provide even more spectral information, which might boost the image for more accurate lithological discrimination.

3.2.5. X-ray diffraction (XRD)

The X Ray Diffraction is considered as one of the most popular analytical techniques for qualitative and quantitative mineralogical composition is X-Ray diffraction. The instrument used is Rigaku SmartLab SE X-Ray diffractometer [60], with measurements ranging between 4 and 90 (2θ) and adopting Brag Brentano geometry, at the center of analysis and characterization, Cadi Ayyad University, Morocco. The results are given in a diffractogram which includes various Bragg's peaks with diverse intensities represented across an experimental axis generally in 2θ degrees [61]. An identification of mineral phases was carried out using paid and free software including High score [62] which identifies the mineral phases, Qualx [63,64] and REX [65] for the refinement (percentages of minerals).

4. Results

4.1. Band ratios

The mineralogical composition was highlighted using ASTER spectral bands and revealed the presence of various kinds of minerals (Table 5). The BR (band6/band8) was able to discriminate amphibole [66–68], which was detected at several areas, such as the sedimentary formations of the Mesozoic (r) and the Cenozoic (s), the pluton of Oussilkane with pyroxene granite and monzogranites, quartz monzonites, and monzo-gabbro-diorites (c), also at the Igoudrane pluton (b) and the Imiter series (andesitic flows) (d). The sericite-illite-smectite were determined using the ratios (band5+band7)/band6 [69], muscovite (band7/band6) [70] as well as phengite (band5/band6) [70] extended at the sedimentary Paleozoic cover (q), the quartz diorites of the Tazzouakt pluton (j), the andesitic flows (d), the granodiorites and tonalites of the Igoudrane pluton (b). The basic degree Index SiO2 used the ratios of (band12/band13) [36,71], where it has a fairly large area, and this were confirmed by the X-Ray diffraction analysis with also the filed survey in which several veins of quartz and acid rocks were found. The Carbonate-Chlorite-epidote with a ratio of (band7+band9)/band 8 [69] is scattered in the western part at the Cenozoic formations (s), the Mesozoic (r), the rhyolitic flows of Jbel Igoudrane (h), the andesitic flows (d), the biotite monzogranite and hornblende (m) and the Oussilkane Pluton (c). The dolomite (band6+band8)/band7 [72] occupies almost the entire study area except the northern Paleozoic structures (q). Moreover, the hydroxide minerals (band6/band2) [73] are largely present in the pluton of Oussilkane (c), the dacitic and andesitic lavas and associated tuffs (n), the ignimbrites, volcanic conglomerates and pyroclastic (o, p), the tonalites of Bou Teglimt pluton (f), the tonalites of Tazzouakt pluton (k), the andesitic flows (d), the Igoudrane pluton (b) and the Paleozoic (q). At last, the ferrous silicates (band5/-band4) [69] we note specially the sedimentary sequences with regional low-grade metamorphism of low Cryogenian (a), the rhyolite flows and domes (h), the biotite monzogranites (m) and the granites and monzo-gabbro diorites of the Oussilkane pluton (c) [Fig. 5 (a-i)].

Rather, the Landsat-8 OLI spectral bands were used to extract alteration minerals including oxidized iron, hydroxides and clay minerals (Table 6). The Ferrous Iron [(band7/band5) + (band3/band4)] [74], the simple Ratio MIR/Red Eisenhydroxid Index (band7/band4) [75] and the ferric oxides (band6/band5) [10,52] almost had a similar extent all over the study area particularly within the granites and mozo-gabbro diorites of Oussilkane pluton (c), the ignimbrites, volcanic conglomerates and pyroclastic (o), the tonalites of Bou Teglimt pluton (f), the andesitic flows (d) and the granodiorites and tonalites of Igoudrane pluton.

Moreover, the BR Red/Blue Iron oxide (band4/band2) [76] is more evident in the granitic formations (c), generally contained in the Ediacaran formations such as the ignimbrites and volcanic conglomerates (e) and the biotite monzogranites (m). The alteration (Laterite) was shown using the BR (band6/band7) [76] and it existed specially in the quartz diorites of Tazzouakt pluton (j), the granites of Oussilkane pluton for and near of the Caldera of Tizi n'Test (i) [Fig. 6 (a-f)].

4.2. PCA, MNF and ICA

Within this research, PCA, MNF along with ICA were selected based on the eigenvectors and eigenvalues of each one of them. The high values of the eigenvectors demonstrated by ASTER are shown in PCA1, PCA2 and PCA3 (Table 2), either the eigenvalues of PCA1

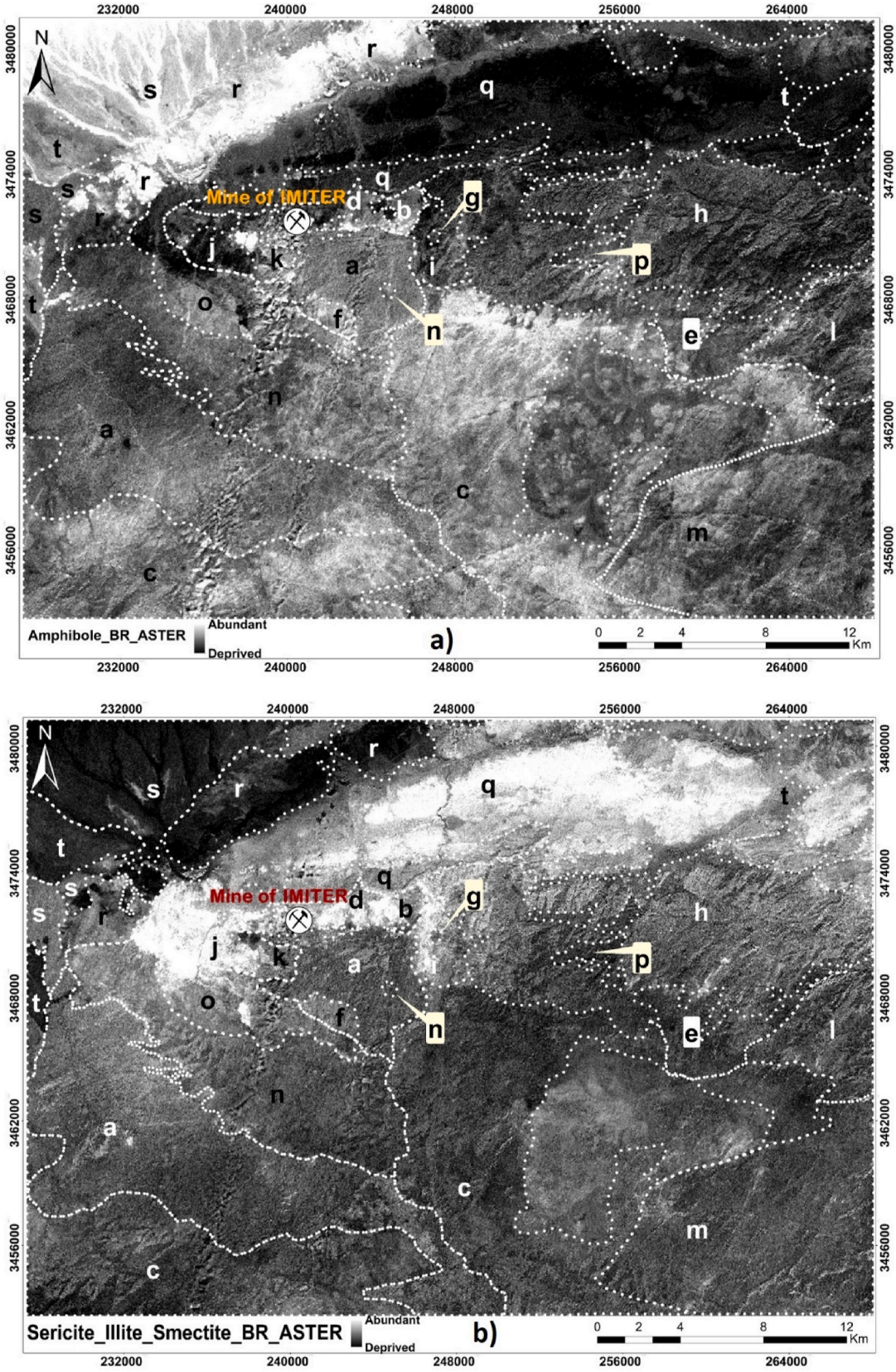

Fig. 5. BR of ASTER sensor: a) Amphibole, b) Sericite-illite-smectite, c) Muscovite, d) Phengite, e) Basic degree index-SiO2, f) Carbonate-chlorite-epidote, g) Dolomite, h) Simple Ratio MIR-Red Eisenhydroxid index, i) Ferrous silicates.

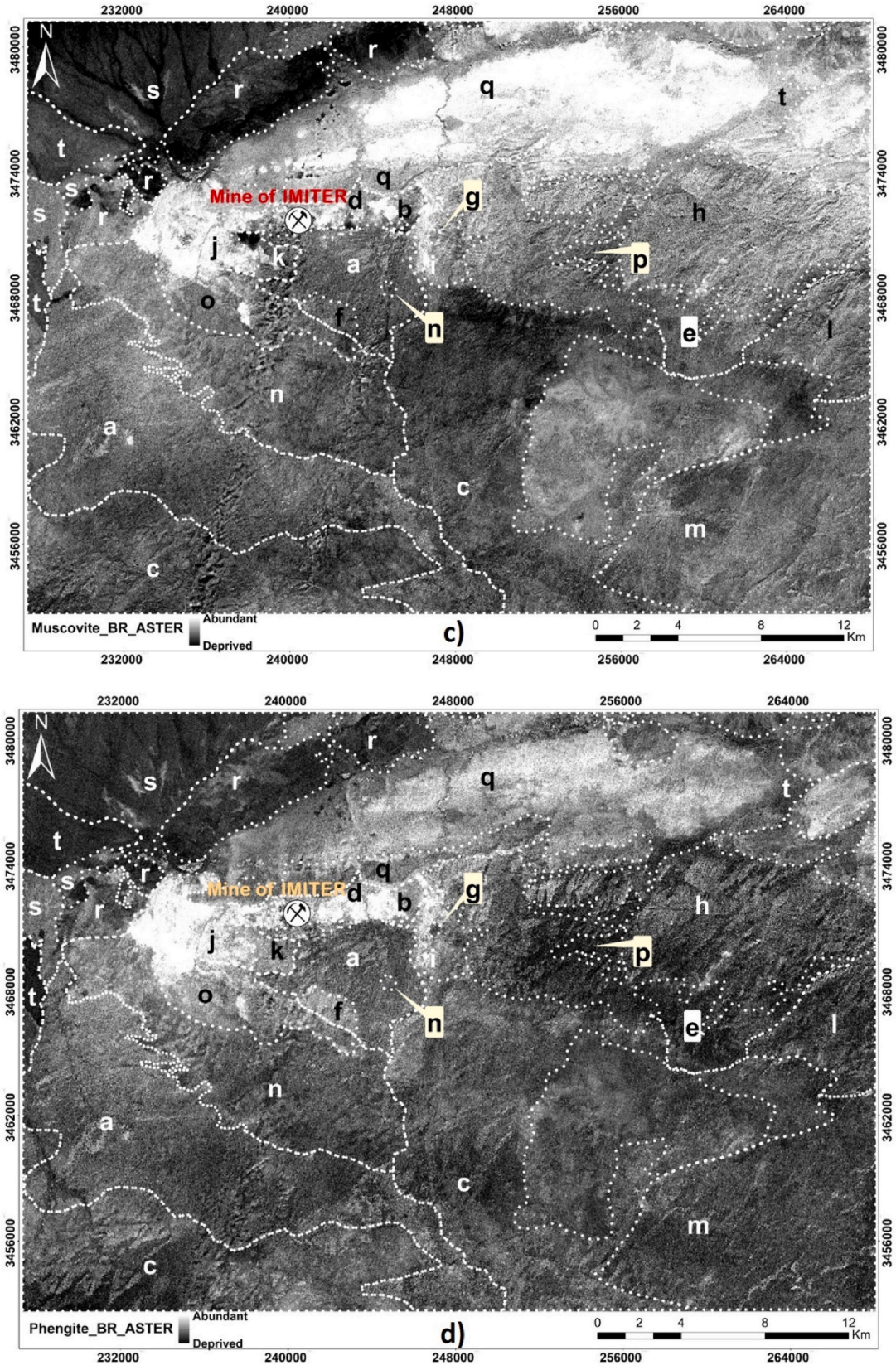

Fig. 5. (*continued*).

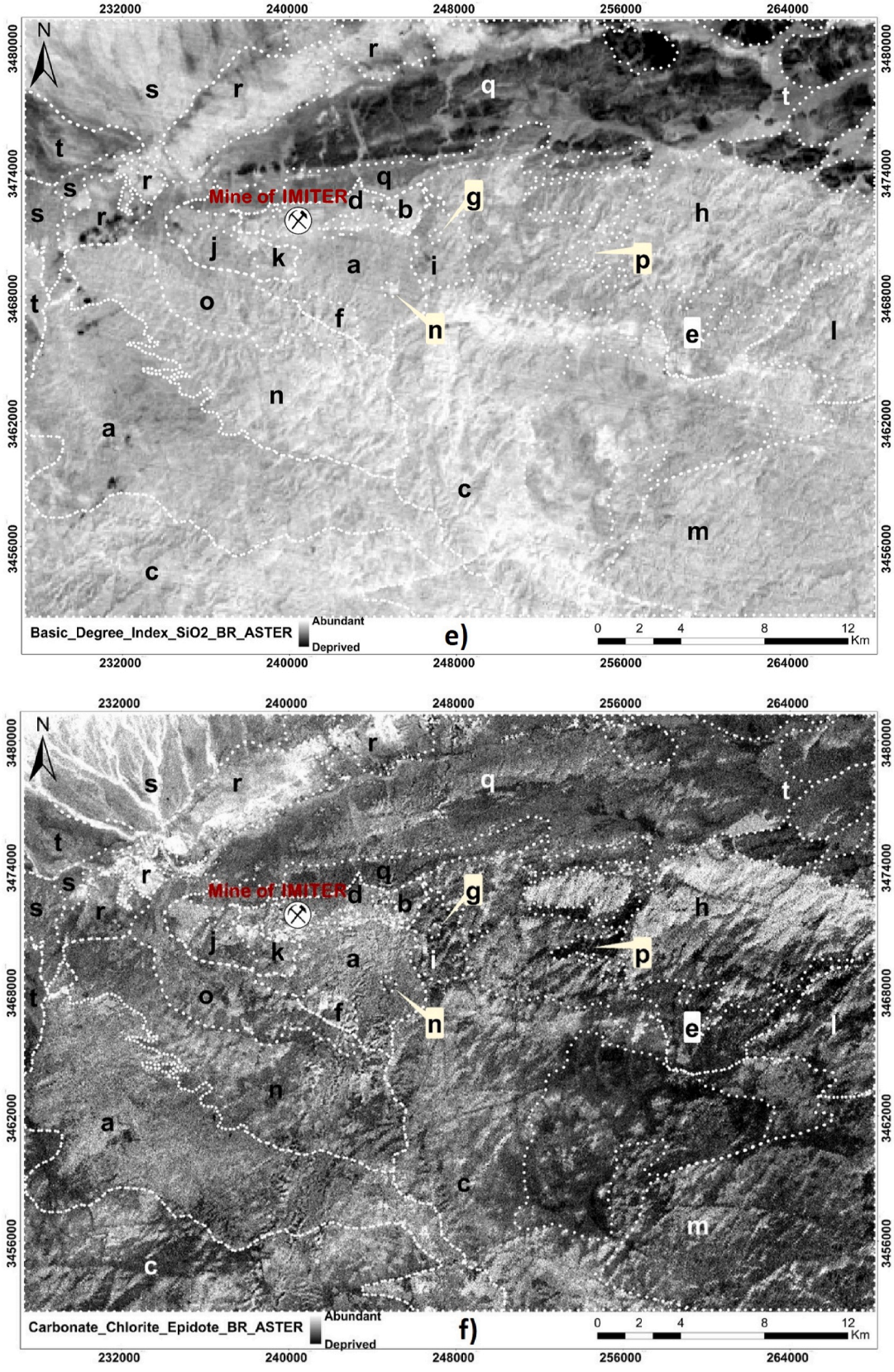

Fig. 5. (*continued*).

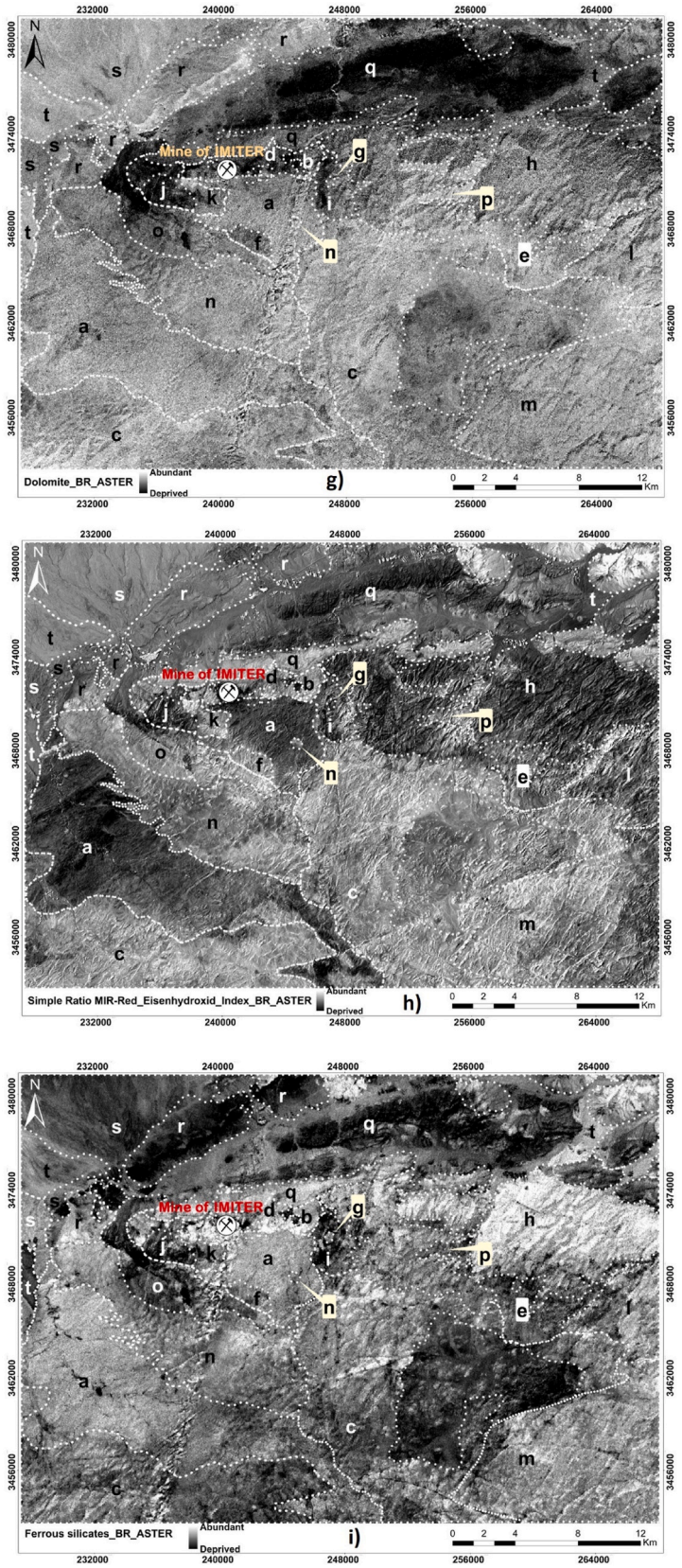

Fig. 5. (*continued*).

Table 6
BR of Landsat-8 OLI sensor.

Mineral	Band Ratios	References
Ferrous Iron	[(band7/band5) + (band3/band4)]	[74]
Simple Ratio MIR-Red Eisenhydroxid index	Band7/band4	[75]
Ferric oxides	Band6/band5	[10,52]
Simple Ratio Red/Blue Iron oxide	Band4/band2	[76]
Alteration/Laterite	(band6/band7)	[76]

have a variance of 93.47%, the PCA2 (4.86%) and PCA3 (0.73%). As a result, allocating the PCA1, PCA2 and PCA3 as an RGB image is the most effective approach to distinguish between the lithologic boundaries. Moreover, the PCA1, PCA2 and PCA3 of Landsat-8 OLI gave the highest eigenvalues (93.58%, 3.23%, 2.73% respectively). Same for MNF and ICA, the first three components were chosen because they have the highest variance (Tables 3 and 4).

For ASTER, the PCA reveal the Cenozoic formations in dark green (s), the sandstone-pelitic formation of Cryogenian (NP2) in purple, the Ediacaran (NP3) in light green (ignimbrite, dacitic and andesitic lavas and even granites). The pluton of Igoudrane and Oussilkane appears in blue and the rhyolitic complex of Ediacaran in orange.

Furthermore, at Landsat-8 OLI the Cenozoic appears in orange, the sandstone-pelitic formation of NP2 in light green, the NP3 appears in dark purple (ignimbrite, dacitic and andesitic lavas and even the granites), the granodiorites and tonalites of Igoudrane pluton and the granites of Oussilkane appears in pink and the rhyolitic complex of NP3 in dark green (h) [Fig. 7 (a, b)].

As well as the MNF and ICA, the previous lithological delimitations are shown besides of having different colors [Fig. 8 (a, b); Fig. 9 (a, b)]. Both of the sensors showed a good discrimination of the lithology in which the results provided are almost the same, beyond of a better visualization of the lithological limits using ASTER.

4.3. XRD

Eight samples were selected for this research, and analyzed with XRD. The diffractograms of the samples highlighted the presence of the crystalline phases [Fig. 10 (a-h)], and the percentages of the minerals were performed using the REX software [65], in order to compare the results with remote sensing fundings. The samples are located in the center of the study area (Fig. 11), and were taken from the sedimentary sequence with regional low-grade metamorphism, gabbro of Igoudrane pluton, the granites of Oussilkane, the conglomerates and sandstones of Imiter series, and rhyolites. After comparing the results of the XRD and the band ratios of the ASTER images, we notice a great resemblance between them, which confirms the study that was made (Tables 7 and 8).

4.4. Reflectance spectrometry

It's an efficient analysis capable of rapidly identifying many alteration minerals. The instrument used is the TerraSpec Halo handheld spectroradiometer [77,78], which has a spectrum range (350–2500 nm) covering the visible/near infrared (VNIR; 350–720 nm) and shortwave infrared (SWIR; 720–2500 nm) [79–81]. The samples don't need any preparation, and measurements can be made directly; the only requirement is that the sample be dry. Minerals that can be identified include phyllosilicates (clays), sorosilicates (epidotes), carbonates (calcite), and some sulfates (alunite) [80]. The results from the Halo handheld spectrometer might be spectral, mineral, or scalar. Scalar values offer details on the sample's composition and/or crystallization, which may be used as additional indicators for probable mineralization [81,82]. Instead of identifying one mineral at a time, TerraSpec Halo offers many predictions with a single reading [83,84].

We analyzed 11 sample during this work, which have the same distribution of the samples treated by XRD. The minerals were detected on the basis of their wavelength absorptions in the VNIR-SWIR regions. The muscovite has an absorption ranging between 2195 and 2215 nm, while phengite is ranging between 2215 and 2225 nm [85]. The illite is known for its deeper absorption at 1900 nm [45]. Two types of chlorites were found in the samples, the Fe–Mg chlorite absorption is varying between 2250 and 2349 nm and the Fe-chlorite with 2256–2360 nm. Iron oxides and hydroxides have at 750, 1000 and 550 nm, where the most common are hematite and goethite [79]. The hornblende has an absorption at 1980 nm, calcite near 2350 nm [83], and 1400 nm as well as 1800 nm characterize the H2O [86] (Fig. 12). The absorption bands seen in the spectra of these rocks are typically those of alteration products or other substitutions, rather than those of the primary association [87].

The results of the BR of ASTER and Landsat-8 OLI were confirmed by the reflectance spectrometry (Tables 9 and 10). As shown clay minerals, oxides and hydroxides such as Goethite, hematite which are largely present in the study area. Attached are field photos of some samples [Fig. 13 (A- D)].

5. Discussion

Remote sensing techniques have been frequently used to successfully map lithological units in mountainous areas where the integration of remote sensing data is greatly useful. A comparison between the transformation methods that were applied (PCA, MNF, ICA) approved the geological formations by grouping the results achieved from Landsat-8 OLI and ASTER images. The lithological

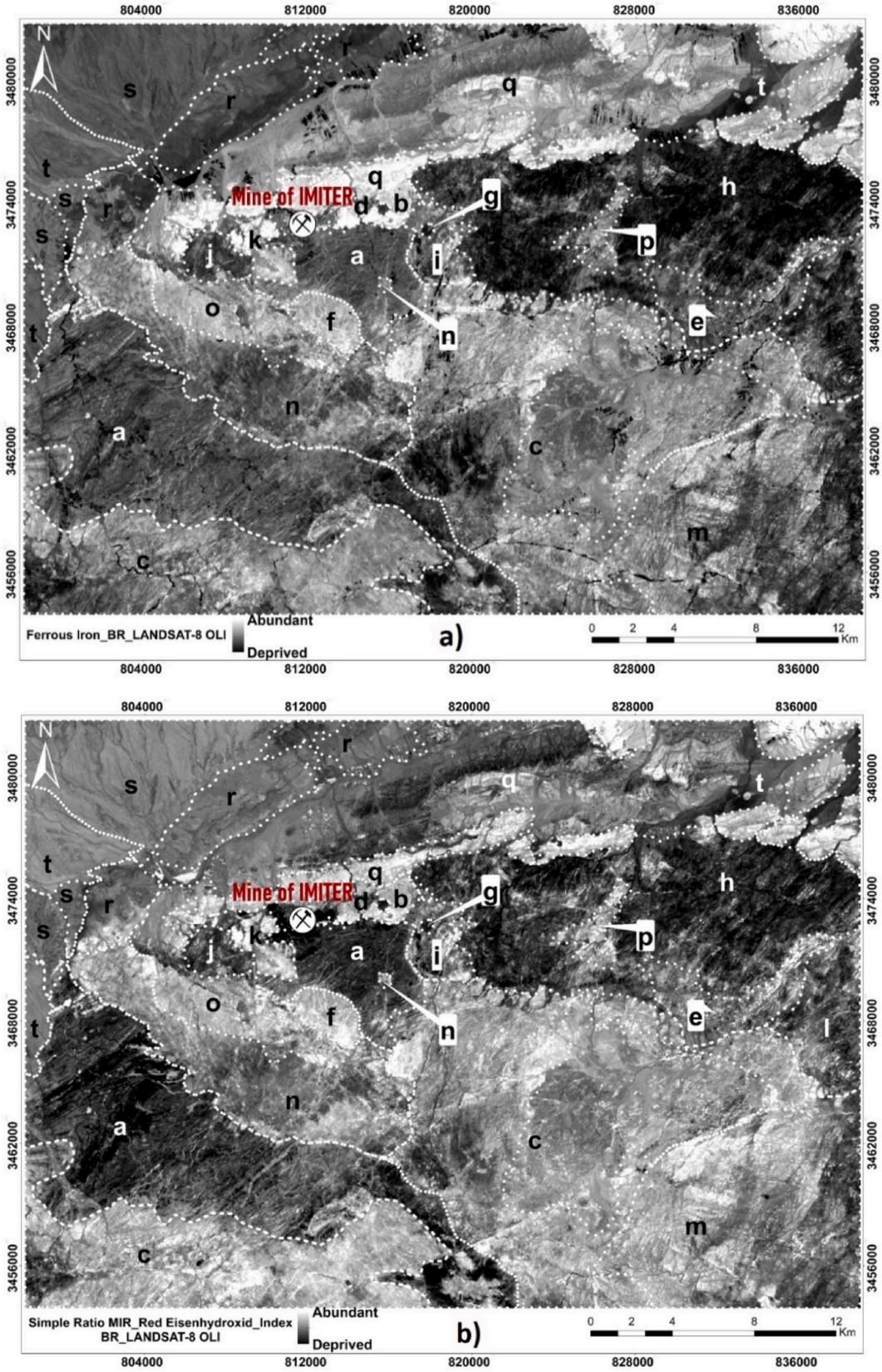

Fig. 6. BR of Landsat-8 OLI sensor: a) Ferrous Iron, b) Simple Ratio MIR-Red Eisenhydroxid index, c) Ferric oxides, d) Simple Ratio Red-Blue Iron oxide, e) Alteration (laterite), f) RGB visualization of (a, b, c) BR.

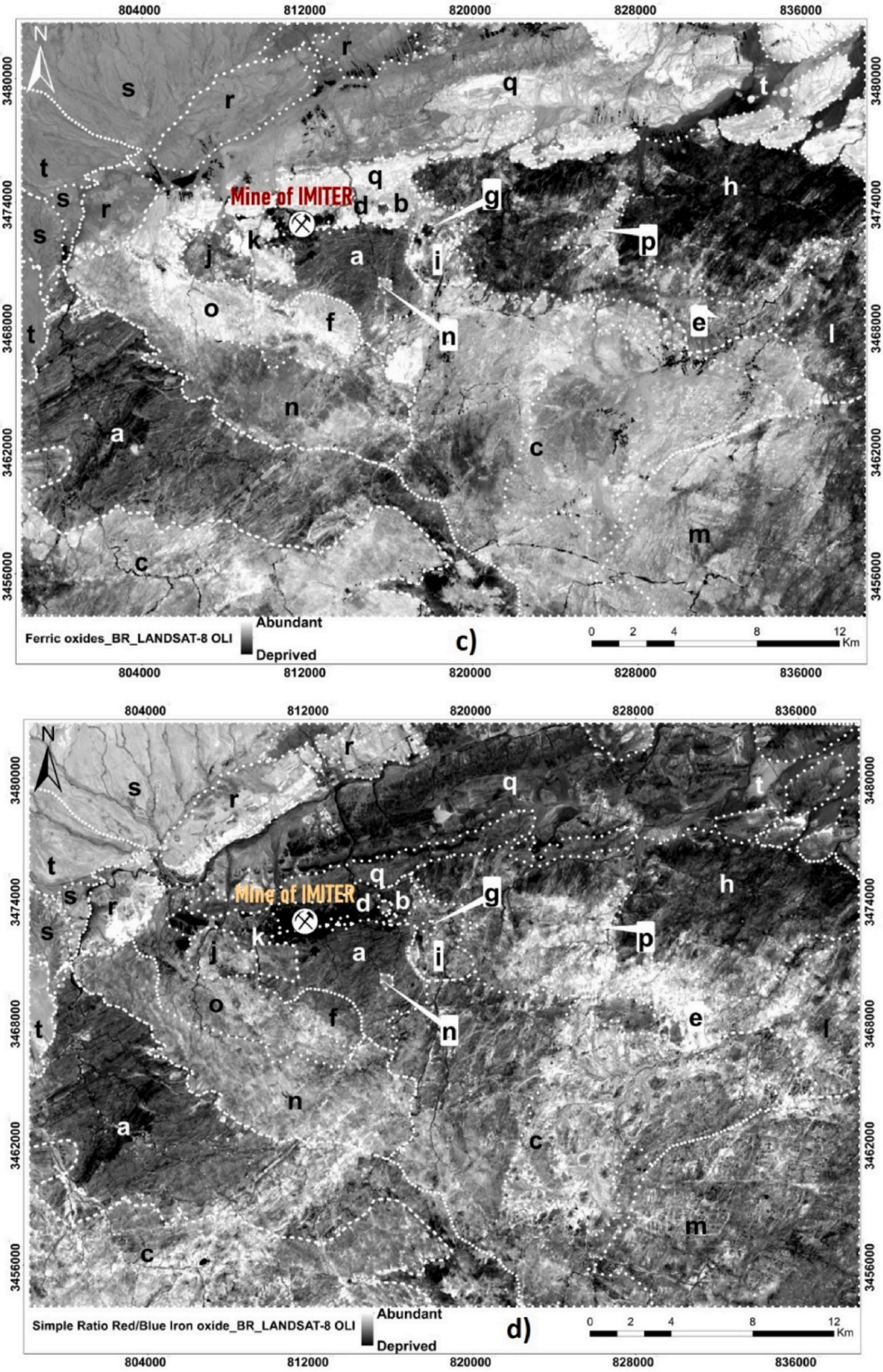

Fig. 6. (*continued*).

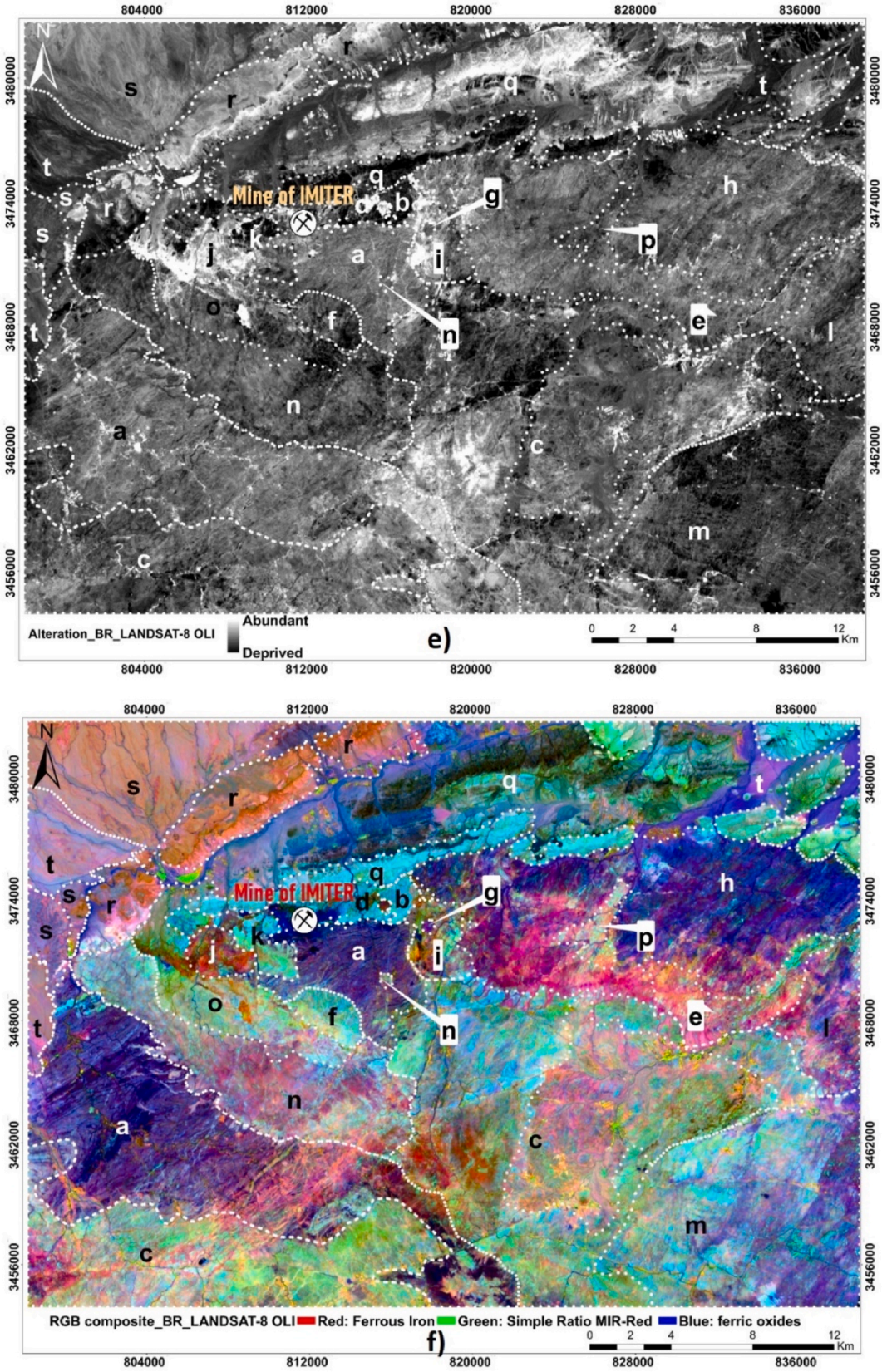

Fig. 6. (*continued*).

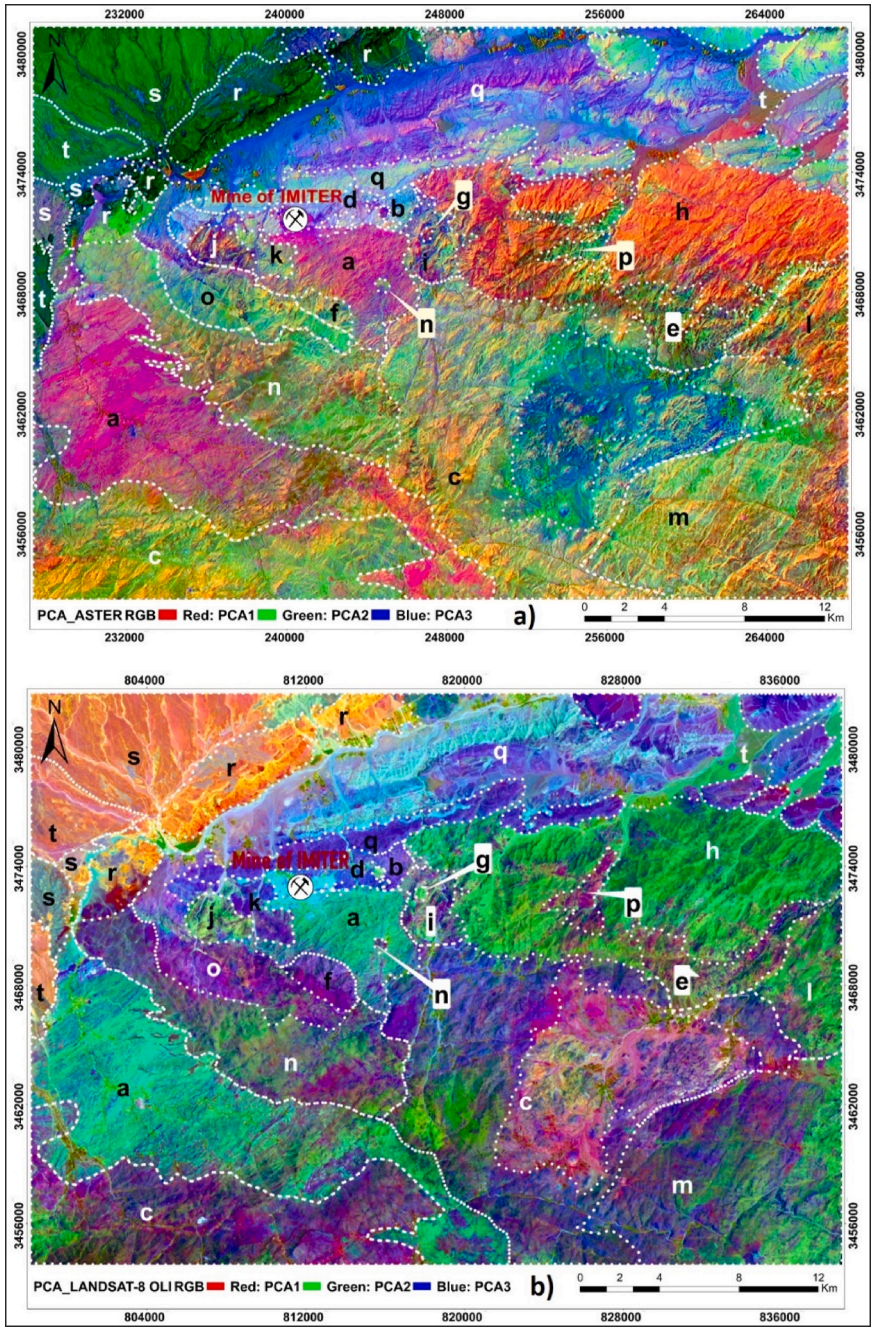

Fig. 7. a) ASTER and b) Landsat-8 OLI PCA1, PCA2, and PCA3 images as an RGB composite.

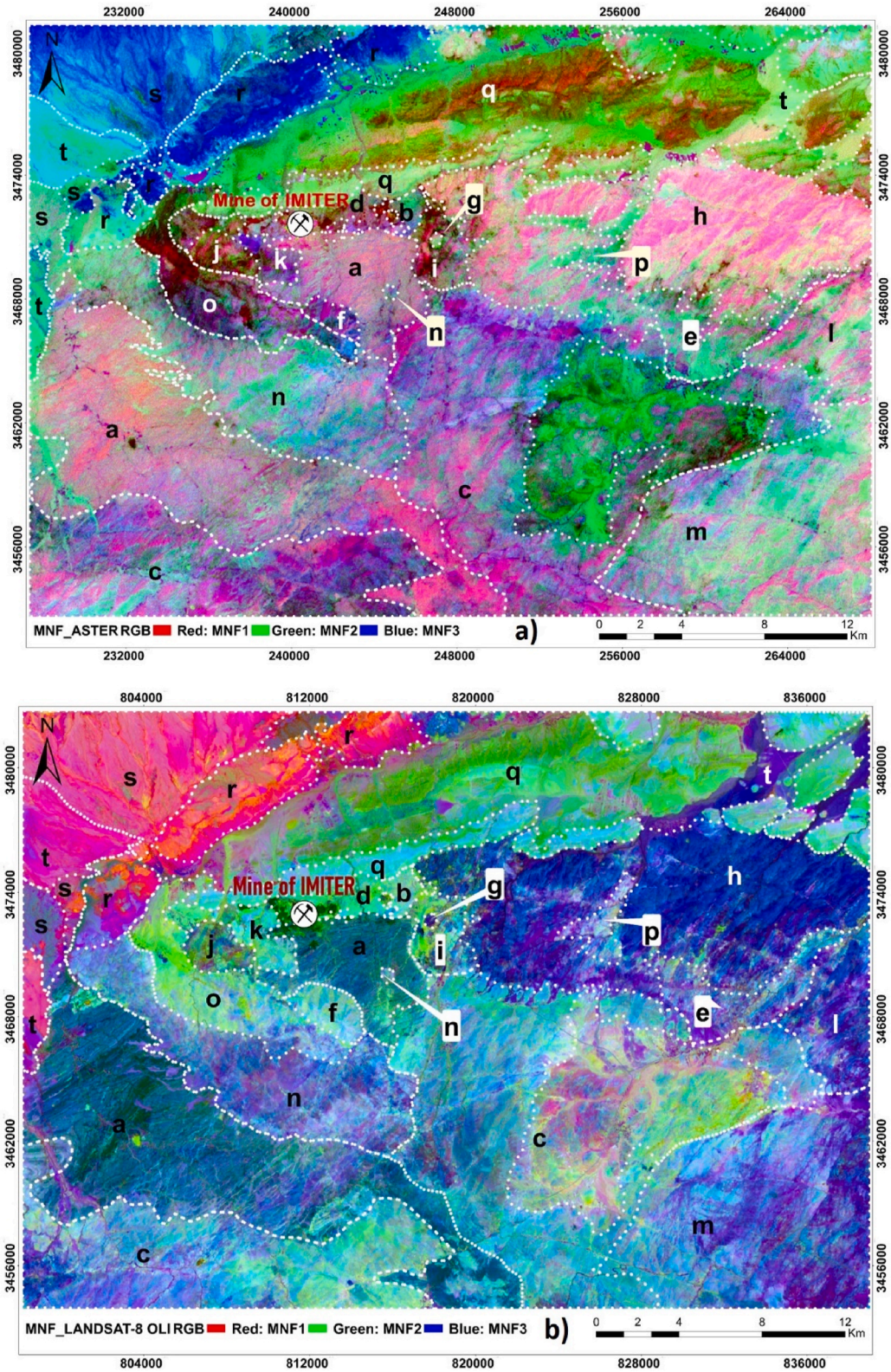

Fig. 8. a) ASTER and b) Landsat-8 OLI MNF1, MNF2, and MNF3 images as an RGB composite.

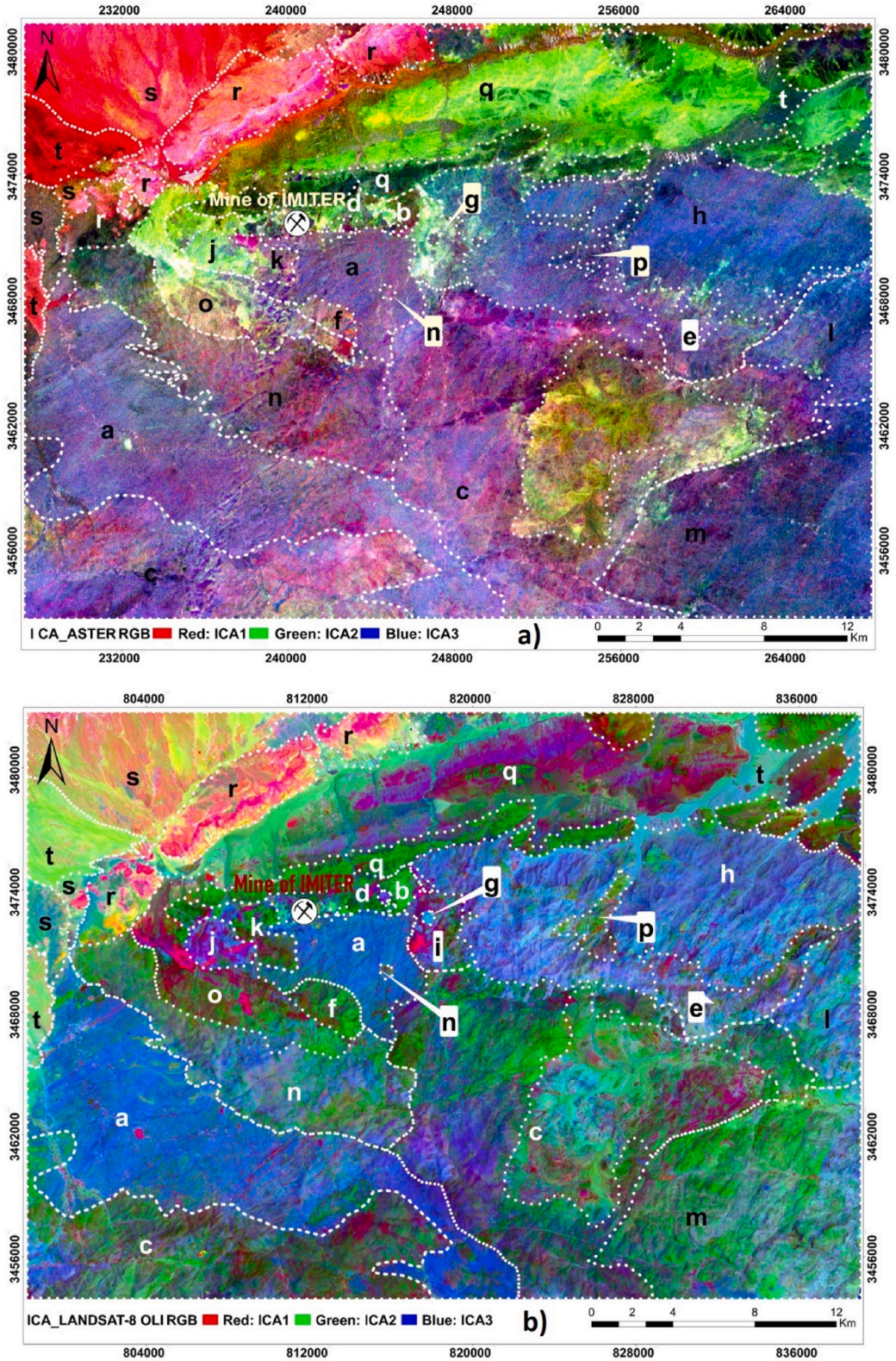

Fig. 9. a) ASTER and b) Landsat-8 OLI ICA1, ICA2, and ICA3 images as an RGB composite.

boundaries were highlighted and each unit were shown separately with a unique color. The two sensors were complementary and gave almost the same result.

The BR used in this research highlighted the existence of several minerals, including amphibole (band6/band8), sericite-illite-smectite [(band5+band7)/6], the SiO2 index (band12/band13), dolomite [(band6+band8)/band7], simple ratio MIR-Red Eisenhydroxid (band6/band2) and ferrous silicates (band5/band4) using ASTER hyperspectral images, and the distribution of these minerals is

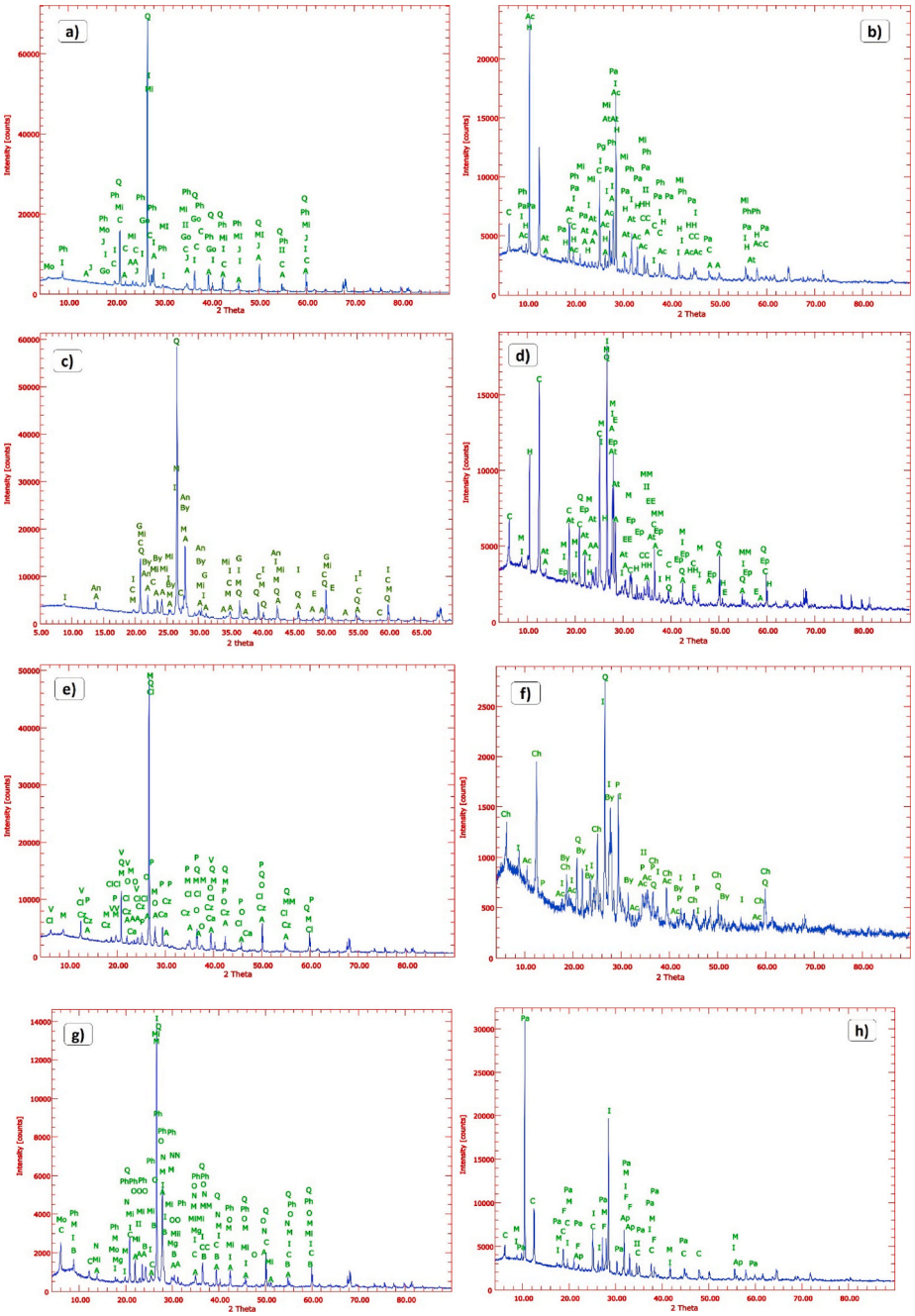

Fig. 10. XRD patterns of targeted samples: a) Altered rhyolite (Average Ediacaran, G15), b) Gabbro and diorites (Upper Cryogenian NP2, G26), c) Rhyolite (Average Ediacaran, G27), d) Gabbro from the Igoudrane Pluton (Upper Cryogenian, G28), e) Pelite (Low Ediacaran, T3), f) Basalt (Upper Cryogenian NP2, T9), g) Formation of Izemgane sandstone-pelitic sediments (NP2i2, T23), h) Gabbro and diorites on the southern edge of the massif (Upper Cryogenian NP2, T49).

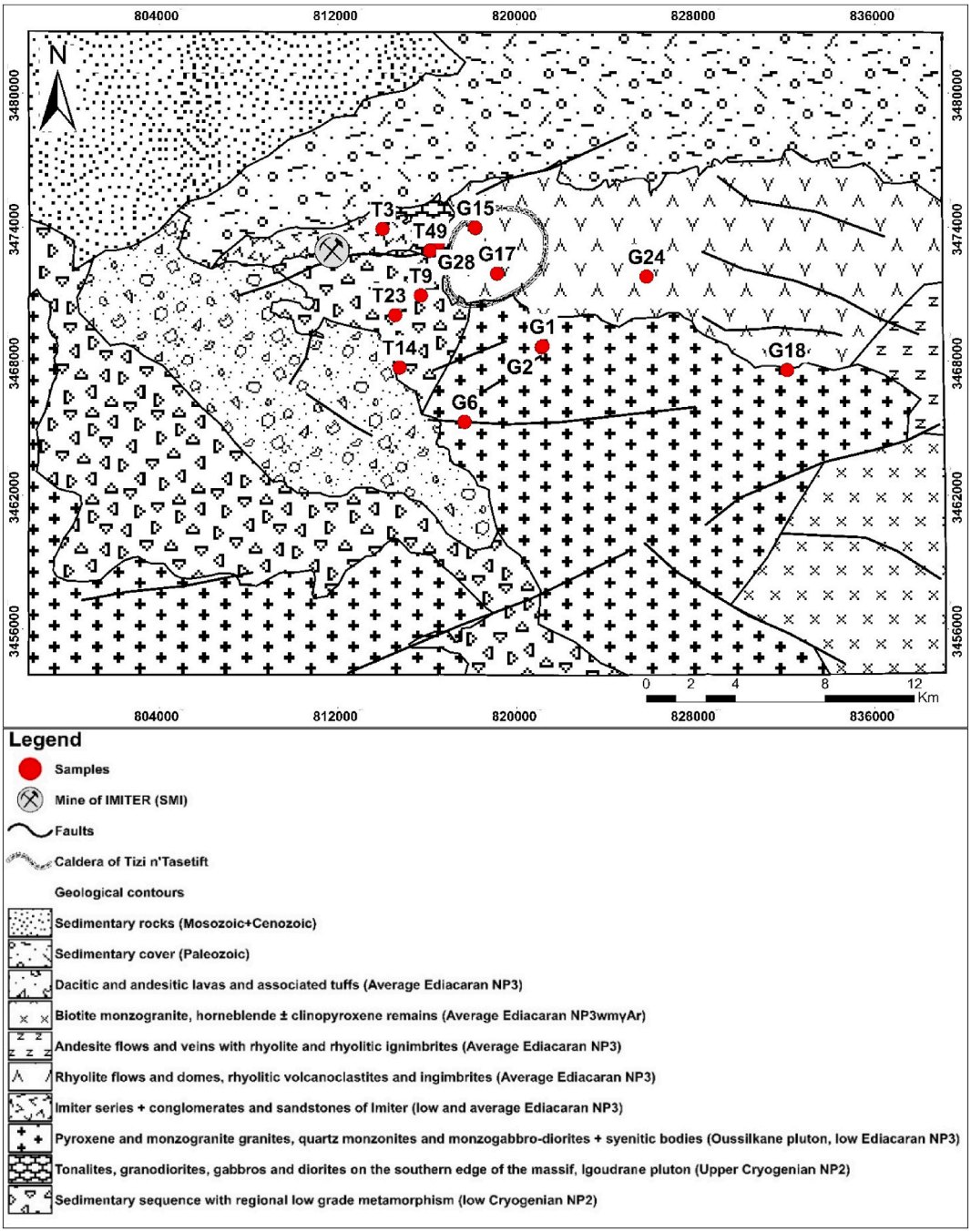

Fig. 11. Lithological map of the Igoudrane region with samples cited in this research.

Table 7
Comparison of mineralogical composition from XRD and results from BR of ASTER sensor.

Samples	G27		T9		T3		T49	
XRD	**Minerals**	**%**	**Minerals**	**%**	**Minerals**	**%**	**Minerals**	**%**
	Illite	3.7	Chlorite	4.08	Clinochlore	13.4	Chlorite	18.19
	Calcite	2.48	Illite	11.94	Vermiculite	1.76	Illite	7.3
	Dolomite	69.71	Anorthite	26.5	Albite	9.69	Muscovite	9.5
	Quartz	13.82	Quartz	12.37	Q Calcite	3.18	Pargasite	55.9
	Ankerite	5.67	Bytownite	19.9	Muscovite	20.87	Fluorapatite	5.12
	Diopside	1.29	Pyroxene	7.09	Quartz	39.4	Apatite	4.05
	Ferrihydrite	0.17	Chamosite	16.51	Chabazite	1.9		
	Chlorite	3.16	Actinolite	1.68	Oligoclase	8.16		
					Pyroxene	1.64		
ASTER	Dolomite		Chlorite-Amphibole		Muscovite		Chlorite-Amphibole	
	Basic degree Index SiO2		Clay minerals (Illite)		Basic degree Index SiO2		Muscovite	
	Clay minerals (Illite)		Basic degree Index SiO2		Carbonate-Chlorite		Clay minerals (Illite)	
	Carbonate-Chlorite		Ferrous silicates		Ferrous silicates			
	Hydroxides				Clay minerals (Vermiculite)			

Table 8
Comparison of mineral phases from XRD and results of ASTER BR.

Samples	T23		G15		G26		G28	
XRD	**Minerals**	**%**	**Minerals**	**%**	**Minerals**	**%**	**Minerals**	**%**
	Chlorite	14.7	Chlorite	1.63	Chlorite	11.44	Illite	7.47
	Illite	12.43	Illite	5.57	Albite	11.09	Albite	22.62
	Albite	17.59	Montmo-rillonite	3.6	Anorthite	7.09	Anorthite	19.21
	Anorthite	23.85	Albite	12.62	Actinolite	3.33	Enstatite	5.52
	Biotite	4.99	Microcline	10.19	Hornblende	42.52	Muscovite	9.6
	Enstatite	2.13	Quartz	46.22	Microcline	9.22	Quartz	16.38
	Muscovite	3.66	Goethite	0.269	Pargasite	2.84	Epidote	3.47
	Quartz	19.48	Jarosite	3.02	Illite	6.95	Hornblende	8.21
	Pyroxene	1.21	Phengite	16.84	Phengite	5.53	Chlorite	7.51
ASTER	Chlorite		Chlorite/hydroxides (Goethite)		Epidote-Chlorite-Amphibole		Muscovite/clay minerals (Illite)	
	Ferrous silicates		Clay minerals (Illite, montmo-rillonite)		Clay minerals (Illite)		Ferrous silicates	
	Muscovite/clay minerals (Illite)		Basic degree Index SiO2		Phengite		Epidote-Chlorite-Amphibole	
	Basic degree Index SiO2		Phengite				Basic degree Index SiO2	

highly compatible with the lithological nature of each geological unit mentioned. The [31] used the same BR employed in this study for argillitic alteration (muscovite and phengite [(band7/band6), (band5/band6)], respectively, and carbonate-chlorite-epidote (band [(band7+band9)/band8)], which was effectively mapped by ASTER SWIR bands. Hydrothermal alteration was common, most notably in the Taghdout Complex, Bou Salda Formation, and Ouarzazate Group, which show alteration areas bearing strongly reflective opaque ore minerals including Cu, Au, Fe, and Ag, as well as magnetite, chlorite, and other phyllosilicates. The [29] exploited the VNIR/SWIR data of ASTER to highlight the presence of chlorite-epidote-amphibole by band4/band8 BR. Kaolinite and other clay minerals, which are alteration products of K-felspar and sericite, were detected with band4/band6 BR. Moreover, PCA9, PCA7, and PCA2 RBG combinations detected alteration halos associated with faults.

In addition, the VNIR-SWIR bands of Landsat-8 OLI highlighted alteration minerals, including ferrous Iron [(band7/band5) +(band3/band4)], hydroxides (band7/band4), ferric oxides (band6/band5), Iron oxide (band4/band2), and alteration-laterite (band6/band7), which are more concentrated at the level of the granitic rocks notably the pluton of Oussilkane, with a concentration of oxides and hydroxides. The [10] mapped the ferric oxides alteration in the Bas Drâa inlier using also the (band6/band5) BR and confirmed the great potential of ASTER data in lithological discrimination, while (band5/band3+band1/band2) BR detected effectively the regions of a high concentration of iron oxides and hydroxide minerals [36].

A classification of all the band ratios were done in order to show the areas in which the minerals highlighted are abundant, with superposition of the combinations (PCA1, PCA2, PCA3), (MNF1, MNF2, MNF3) and (ICA1, ICA2, ICA3) of ASTER images and Landsat-8 OLI (Fig. 14). The [30] demonstrated that the SAM and SID classifications are effective for discriminating granitoids based on differences in the amount of silica. MLC algorithms effectively identified Proterozoic basement formations and contacts between metamorphic stones, granitoids, and carbonate cover surrounding the Iguerda inlier. The remote sensing techniques used in this study, in conjunction with field observations and petrographic analyses, clearly show that hyperspectral analysis of ASTER data offers detailed lithologic discrimination that improves field mapping of metamorphic basements, especially in the arid areas of the Moroccan Anti-Atlas. The Precambrian basement and the Ediacaran-Cambrian cover can be easily distinguished by hyperspectral analysis of

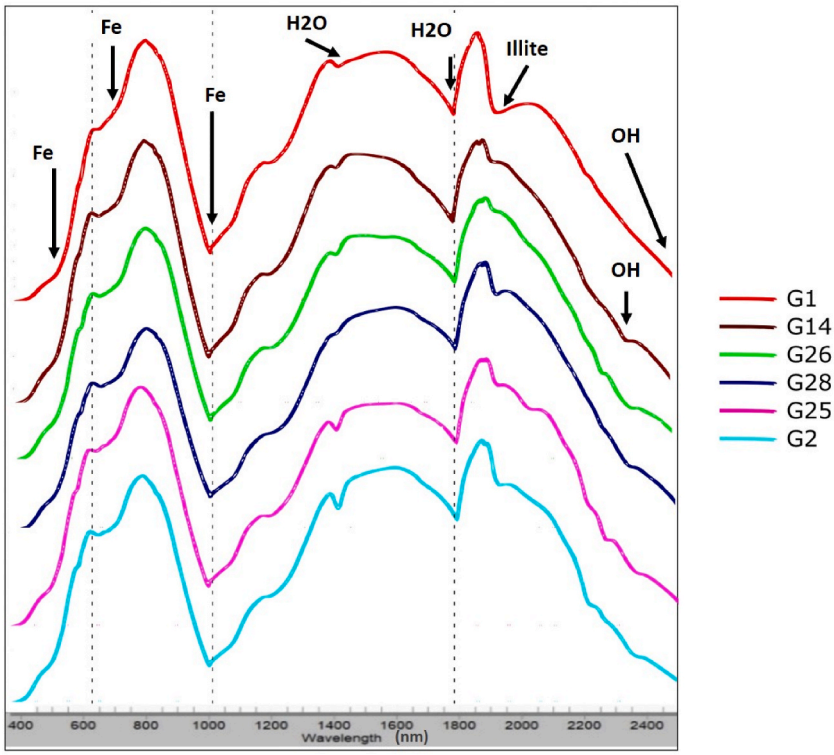

Fig. 12. Spectral profiles of representative samples obtained from reflectance spectrometry.

Table 9
Comparison of reflectance spectrometry alteration minerals and results of Landsat-8 OLI BR.

Samples	G1	G6	G10	G17	G24	T14
Reflectance spectrometry	Goethite Chabazite Montmo-rillonite FeMg-Chlorite Hematite	Goethite Chabazite Montmo-rillonite Clinozoisite	Hematite Chabazite Mg-Illite Goethite	Hematite Mg-Illite Fe-chlorite Ferro-actinolite FeMg-chlorite	Hematite Iron Saponite Montmo-rillonite Kaolinite	Goethite K-Illite Vermiculite Fe-Chlorite
Landsat-8 OLI	Alteration/Simple Ratio Red-Blue Iron oxides Ferric oxides/Ferrous Iron/Simple Ratio MIR-Red Eisenhydroxid Index					

Table 10
Comparison of reflectance spectrometry alteration minerals and results of ASTER BR.

Samples	G2	G14	G25	G26	G28
Reflectance spectrometry	Mg-Illite Chabazite K-Illite/Lepidolite FeMg-Chlorite	Calcite Mg-Illite Fe-chlorite	Fe–Mg chlorite Muscovite Mg-Illite	Phengite K-Illite Fe–Mg chlorite Hornblende	Mg-Illite Epidote Lepidolite
ASTER	Carbonate-Chlorite-Epidote/Phengite Amphibole/Muscovite/Illite				

ASTER data. Landsat-8 OLI helped to identify the different geological formations of the Oumjrane–Boukerzia mining district, and PCA1, PCA4, PCA3 RGB composite provided a good discrimination [34]. Another comparison between ASTER and Landsat-8 OLI for lithological discrimination was done in the eastern Anti-Atlas of Morocco by Marzouki (2023) [35]. They used PCA (653 and 821), MNF (643 and 541), as well as ICA (137 and 235) to distinguish between the formations, such as the granitic, the rhyolitic and the ignimbritic ones. The classification based on ASTER images showed accuracy, and the ASTER was evaluated the best for lithological discrimination. The XRD and reflectance spectrometry analyses, showed a similar result as the one determined by remote sensing, either for minerals from ASTER or Landsat-8 OLI BR.

Fig. 13. Pelites and diorite alternance alongside bioturbation (Low Ediacaran NP3, T3) [A, B]/Gabbro and diorites on the southern edge of the massif (Upper Cryogenian NP2, T49) [C]/Pink granite (Oussilkane pluton, low Ediacaran NP3, G1) [D].

6. Conclusion

This study used the multispectral images of ASTER and Landsat-8 OLI, which were employed to delimit the existing geological formations within the Igoudrane study region, together with mineralogical mapping. The SWIR and VNIR bands of both of the sensors were exploited by adopting several techniques (BR, PCA, MNF, ICA, and classification). The analysis of the previous results provided that ASTER and Landsat-8 OLI possess an appreciable result in lithological discrimination, where we were clearly able to delineate the different geological units, showing a different color for each of them, with a validation using the geological map of Imtir (1/50 000) alongside a field survey. ASTER provided more information in mineralogical mapping because of its number of bands and the spectral richness in the SWIR regions, while Landsat-8 OLI highlighted more oxidation. The BR and their classification gave us the spatial distribution of several minerals, amphibole, illite, smectite, muscovite, phengite, basic degree index SiO2, calcite, chlorite, epidote, dolomite, hydroxides, and ferrous silicates were identified throughout the BR measured with ASTER. Landsat-8 OLI BR also revealed areas containing oxides, hydroxides, and laterite. The spectral profiles were extracted using the IGCP library and resampled to ASTER and Landsat-8 OLI, and revealed these minerals according to their absorption in the VNIR and SWIR areas. Al–OH absorption at 2.20 μm distinguishes muscovite and illite (phyllic alteration). Muscovite, illite, and Kaolinite are also constituents of the argillitic alteration, with Kaolinite having a significant absorption at 0.9 μm. The propylitic alteration zone was characterized by chlorite and carbonates, with absorption ranging between 2.3 μm and 2.35 μm according to CO3 and Mg–OH compositions.

The oxidation (hematite and jarosite) was characterized by absorption near 0.95 μm and 2.3 μm, respectively, whereas the goethite spectral profile shows absorption near 1.4 μm and 2.2 μm, respectively. Smectite absorbs at 1.4 μm and near 2.2 μm. The absorption of amphibole was between 1.4 μm and 2.3 μm, while that of pyroxene was near 1.4 μm and 2.3 μm. The choice of the PCA, MNF and ICA was based on their eigenvectors and eigenvalues, where the first three components of ASTER and Landsat-8 OLI had the highest values, and provided significant lithology discrimination, particularly with ASTER.

For ASTER, the PCA1, PCA2, and PCA3 has as eigenvalue 99.06%, 93.87% for MNF1, MNF2, and MNF3. The ICA1, ICA2, and ICA3 with 99.05%. Landsat-8 OLI showed 99.54% as eigenvalue for PCA1, PCA2, and PCA3. 84.5% for MNF1, MNF2, and MNF3, and 99.05% for ICA1, ICA2, and ICA3. Furthermore, the XRD quantified the mineralogy of the rocks, which were compared to ASTER's BR. The reflectance spectrometry highlighted alteration minerals that showed a high complementarity with the BR applied, such as muscovite (2195–2215 nm), phengite (2215–2225 nm), illite (1900 nm), Fe–Mg chlorite (2250–2349 nm), Fe-chlorite (2256–2360 nm), iron oxides/hydroxides (750–1000 nm and 550 nm), hornblende (1980 nm), and calcite (2350 nm).

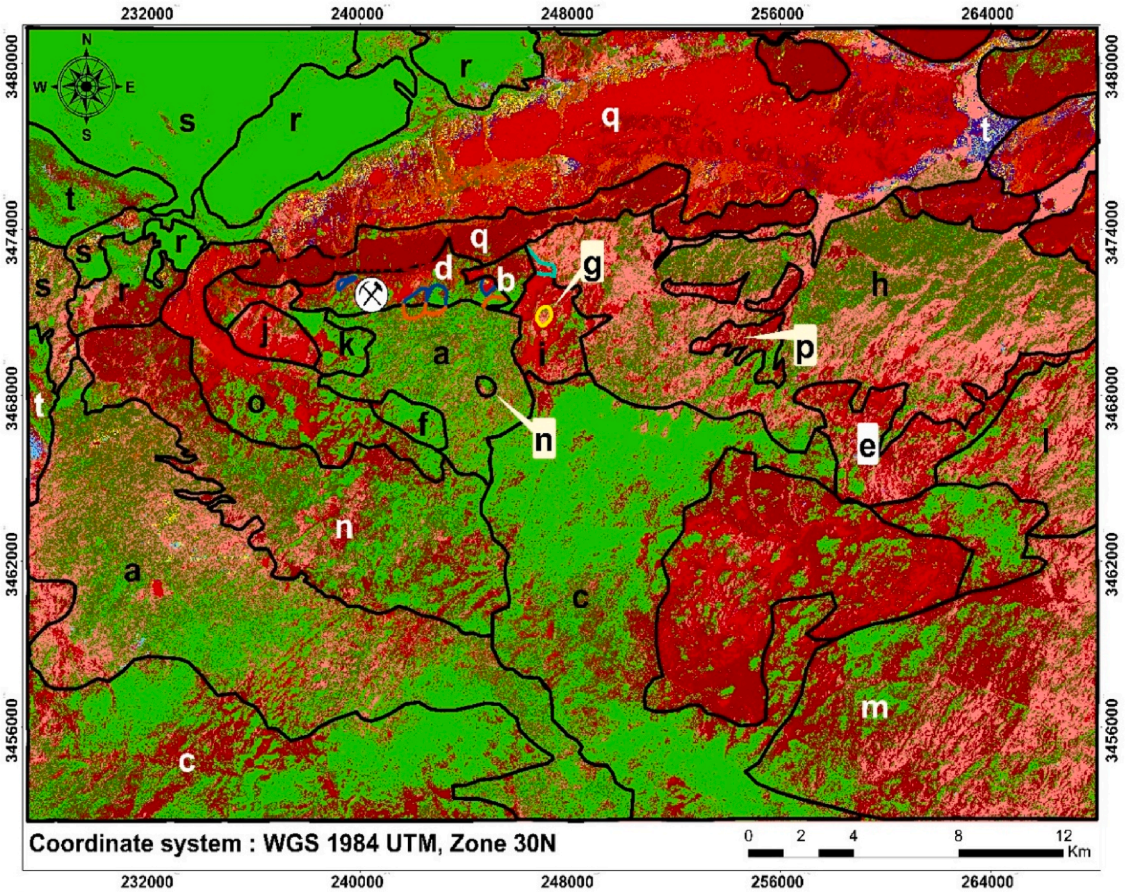

Legend

Mine of IMITER (SMI)

Geological contours

- t : Quaternary
- s : Cenozoic sedimentary rocks
- r : Mesozoic
- q : Sedimentary Paleozoic cover
- p : Ignimbrites, volcanic conglomerates and pyroclastics (Upper Ediacaran NP3ws2)
- o : Ignimbrites, volcanic conglomerates and pyroclastics ('Upper Ediacaran NP3ws1b)
- n : Dacitic and andesitic lavas and associated tuffs (Average Ediacaran NP3wm1), (570±7Ma)
- m : Biotite monzogranite, hornblende ± clinopyroxene remains (Average Ediacaran NP3wmγAr),(571±22Ma)
- l : Andesite flows and veins with rhyolite and rhyolitic ignimbrites (Average Ediacaran NP3wm2b)
- k : Tonalites (Average Ediacaran NP3wmΔTz, Tazzouakt pluton)
- j : Quartz diorites, (Average Ediacaran NP3wmγTz, Tazzouakt Pluton) (572-569Ma)
- i : Caldera of Tizi n'Test (Average Ediacaran NP3wm6a)
- h : Rhyolite flows and domes, rhyolitic volcanoclastites and ingimbrites (Average Ediacaran NP3wm6a)
- g : Circular shape appears at the rhyolitic Caldera of Tizi n'Test NP3
- f :Tonalites often rich in dark enclaves, Bou Teglimt pluton (Average Ediacaran NP3wmΔBt)
- e : Ignimbrites, volcanic conglomerates and pyroclastics (Average Ediacaran NP3wm2a)
- Alternating lavas and rhyolitic tuffs, Imiter series (Average Ediacaran NP3wm)
- Flows, ignimbrites and rhyolitic breccias, Imiter series (Low Ediacaran NP3wi1c)
- d : Andesitic flows, imiter series (low Ediacaran NP3wi1a)
- c : Oussilkane pluton (Low Ediacaran NP3)
- Conglomerates and sandstones of Imiter (Basal Ediacaran NP3Wb)
- b : Igoudrane pluton (Upper Cryogenian NP2)
- a: Sedimentary sequence with regional low grade metamorphism (Low Cryogenian NP2)

Amphibole	Sericite_Muscovite_Illite_Smectite
Amphibole_MgOH	Ferrous_silicates
Simple_Ratio_MIR_RED Eisenhydroxid_Index	Dolomite
Alteration / Laterite	Phengite
Ferrous_Iron	Ferric_oxides
Basic_degree_Index_SiO2	Kaolinite
Carbonate_Chlorite_Epidote	Carbonate
Muscovite	Alunite_Kaolinite_Pyrophylite

(caption on next page)

Fig. 14. Summary map of geologic formation boundaries and mineralogy distribution based on ASTER and Landsat-8 OLI image results from PCA, MNF, ICA, and classified BR.

The limitations of the methodology adopted during this work could be summarized as follows: The XRD is a method for quantifying the minerals present in the stones, and we still need to study the thin sections of the samples to improve their mineralogy; the spectral profiles extracted from the IGCP library are more explicative than the resampled ones, and it's due to several factors, in which the resolution of the image is very important; the reflectance spectrometry is more suitable because we could define the alteration minerals present in the rocks along with spectral profiles. In conclusion, the methodology was efficient and may be adapted in arid regions with less vegetation.

Author contribution statement

Baid Soukaina: Conceived and designed the experiments; Performed the experiments; Analyzed and interpreted the data; Wrote the paper.

Tabit Abdelhalim; Algouti Ahmed; Elghouat Akram; Ezzahzi Salma: Contributed reagents, materials, analysis tools or data.

Algouti Abdellah: Analyzed and interpreted the data; Contributed reagents, materials, analysis tools or data.

Nafouri Imane: Performed the experiments.

Souddi Saber; Aboulfaraj Abdelfattah: Conceived and designed the experiments.

Data availability statement

Data will be made available on request.

Declaration of competing interest

The authors declare that they have no known competing financial interests or personal relationships that could have appeared to influence the work reported in this paper.

References

[1] D.W. Leverington, W.M. Moon, Landsat-TM-based discrimination of lithological units associated with the Purtuniq ophiolite, Quebec, Canada, Rem. Sens. 4 (5) (2012) 1208–1231.
[2] M. Pournamdari, M. Hashim, A.B. Pour, Spectral transformation of ASTER and Landsat TM bands for lithological mapping of Soghan ophiolite complex, south Iran, Adv. Space Res. 54 (4) (2014) 694–709.
[3] R. Frutuoso, A. Lima, A.C. Teodoro, Application of remote sensing data in gold exploration: targeting hydrothermal alteration using Landsat 8 imagery in northern Portugal, Arabian J. Geosci. 14 (2021) 1–18.
[4] I. Bachri, M. Hakdaoui, M. Raji, A.C. Teodoro, A. Benbouziane, Machine learning algorithms for automatic lithological mapping using remote sensing data: a case study from Souk Arbaa Sahel, Sidi Ifni Inlier, Western Anti-Atlas, Morocco, ISPRS Int. J. Geo-Inf. 8 (6) (2019) 248.
[5] T. Zhang, et al., Integrating data of ASTER and Landsat-8 OLI (AO) for hydrothermal alteration mineral mapping in duolong porphyry cu-au deposit, Tibetan Plateau, China, Rem. Sens. 8 (11) (2016) 890.
[6] J.C. Mars, Hydrothermal Alteration Maps of the Central and Southern Basin and Range Province of the United States Compiled from Advanced Spaceborne Thermal Emission and Reflection Radiometer (ASTER) Data, 2012.
[7] T. Timkin, M. Abedini, M. Ziaii, M.R. Ghasemi, Geochemical and hydrothermal alteration patterns of the abrisham-rud porphyry copper district, semnan province, Iran, Minerals 12 (1) (2022) 103.
[8] H. Ahmadi, E. Pekkan, Fault-based geological lineaments extraction using remote sensing and GIS—a review, Geosciences 11 (5) (2021) 183.
[9] M. Abrams, et al., The advanced spaceborne thermal emission and reflection radiometer (ASTER) after fifteen years: review of global products, Int. J. Appl. Earth Obs. Geoinf. 38 (2015) 292–301.
[10] Z. Adiri, A. El Harti, A. Jellouli, L. Maacha, E.M. Bachaoui, Lithological mapping using landsat 8 OLI and terra ASTER multispectral data in the Bas Drâa inlier, Moroccan anti atlas, J. Appl. Remote Sens. 10 (1) (2016), 16005.
[11] S. Gad, T. Kusky, ASTER spectral ratioing for lithological mapping in the Arabian–Nubian shield, the Neoproterozoic Wadi Kid area, Sinai, Egypt, Gondwana Res. 11 (3) (2007) 326–335.
[12] G.R. Hunt, Spectral signatures of particulate minerals in the visible and near infrared, Geophysics 42 (3) (1977) 501–513.
[13] A.B. Pour, M. Hashim, The application of ASTER remote sensing data to porphyry copper and epithermal gold deposits, Ore Geol. Rev. 44 (2012) 1–9.
[14] S. Grebby, D. Cunningham, K. Tansey, J. Naden, The impact of vegetation on lithological mapping using airborne multispectral data: a case study for the north Troodos region, Cyprus, Rem. Sens. 6 (11) (2014) 10860–10887.
[15] A. Beiranvand Pour, M. Hashim, ASTER, ALI and Hyperion sensors data for lithological mapping and ore minerals exploration, SpringerPlus 3 (2014) 1–19.
[16] D. Santos, J. Cardoso-Fernandes, A. Lima, A. Müller, M. Brönner, A.C. Teodoro, Spectral analysis to improve inputs to random forest and other boosted ensemble tree-based algorithms for detecting NYF pegmatites in Tysfjord, Norway, Rem. Sens. 14 (15) (2022) 3532.
[17] M. Köhler, et al., Lithium potential mapping using artificial neural networks: a case study from central Portugal, Minerals 11 (10) (2021) 1046.
[18] H. Azizi, M.A. Tarverdi, A. Akbarpour, Extraction of hydrothermal alterations from ASTER SWIR data from east Zanjan, northern Iran, Adv. Space Res. 46 (1) (2010) 99–109.
[19] Y. Ninomiya, B. Fu, Regional lithological mapping using ASTER-TIR data: case study for the Tibetan Plateau and the surrounding area, Geosciences 6 (3) (2016) 39.
[20] Y. Sakamoto, et al., Development and flight results of microsatellite bus system for RISING-2, Trans. Japan Soc. Aeronaut. Sp. Sci. Aerosp. Technol. Japan 14 (2016) ists30, p. Pf_89-Pf_96.
[21] J. Cardoso-Fernandes, A.C. Teodoro, A. Lima, Remote sensing data in lithium (Li) exploration: a new approach for the detection of Li-bearing pegmatites, Int. J. Appl. Earth Obs. Geoinf. 76 (2019) 10–25.
[22] A.M. Eldosouky, R.A.Y. El-Qassas, A.B. Pour, H. Mohamed, M. Sekandari, Integration of ASTER satellite imagery and 3D inversion of aeromagnetic data for deep mineral exploration, Adv. Space Res. 68 (9) (2021) 3641–3662.

[23] S. Guha, H. Govil, Evaluation of ASTER TIR data-based lithological indices in malanjkhand copper mines of Madhya Pradesh, India, B. Appl. Earth Sci. 129 (1) (2020) 3–8.
[24] Y. Song, P. Wang, C. Lian, B. Wang, Lithologic mapping and alteration information extracting based on ASTER spectral signature: an example from nianzha gold deposit, Northwest. Geol. 54 (2) (2021) 126–136.
[25] A.E.A. El Fels, M. El Ghorfi, Using remote sensing data for geological mapping in semi-arid environment: a machine learning approach, Earth Sci. Informatics 15 (1) (2022) 485–496.
[26] A. Forouzesh, Z. Bonyadi, Extraction of alteration minerals spectra in Angouran zinc and lead deposits using ASTER image processing, Adv. Appl. Geol. 2 (2022) 7662–7722.
[27] R. Moradi, M. Boomeri, Remote sensing detection of altered zones associated with Cu-Mo mineralization in North of Zahedan, SE Iran using Landsat-8 data, Yerbilimleri 38 (3) (2017) 275–294.
[28] O.O. Osinowo, A. Gomy, M. Isseini, Mapping hydrothermal alteration mineral deposits from landsat 8 satellite data in Pala, mayo Kebbi region, southwestern Chad, Sci. African 11 (2021), e00687.
[29] M. Massironi, et al., Interpretation and processing of ASTER data for geological mapping and granitoids detection in the Saghro massif (eastern Anti-Atlas, Morocco) interpretation of ASTER data for geological mapping and granitoids detection, Geosphere 4 (4) (2008) 736–759.
[30] M. El Janati, A. Soulaimani, H. Admou, N. Youbi, A. Hafid, K.P. Hefferan, Application of ASTER remote sensing data to geological mapping of basement domains in arid regions: a case study from the Central Anti-Atlas, Iguerda inlier, Morocco, Arabian J. Geosci. 7 (2014) 2407–2422.
[31] M. El Janati, Application of remotely sensed ASTER data in detecting alteration hosting Cu, Ag and Au bearing mineralized zones in Taghdout area, Central Anti-Atlas of Morocco, J. Afr. Earth Sci. 151 (2019) 95–106.
[32] A. Jellouli, A. El Harti, Z. Adiri, E.M. Bachaoui, A. El Ghmari, Application of remote sensing data in lithological discrimination of kerdous inlier in the anti atlas belt of Morocco, JOIV Int. J. Informatics Vis. 3 (2–2) (2019) 227–232.
[33] Z. Adiri, et al., Mineralogical mapping using landsat-8 OLI, terra ASTER and sentinel-2A multispectral data in Sidi flah-bouskour inlier, Moroccan anti-atlas, J. Spat. Sci. 65 (1) (2020) 147–171.
[34] O. Lhoussayn, G. Abdessamad, L. Benaissi, B. Es-sabbar, S.M. Hicham, Lithostructural mapping using landsat OLI images and field investigations in the oumjrane–boukerzia mining district, eastern anti-atlas, Morocco, Iraqi Geol. J. (2022) 14–33.
[35] A. Marzouki, A. Dridri, Lithological discrimination and structural lineaments extraction using Landsat 8 and ASTER data: a case study of Tiwit (Anti-Atlas, Morocco), Environ. Earth Sci. 82 (5) (2023) 125.
[36] L. Ouhoussa, A. Ghafiri, L. Ben Aissi, B. Es-Sabbar, Integrating aster images processing and fieldwork for identification of hydrothermal alteration zones at the oumjrane-boukerzia district, Moroccan anti-atlas, Open J. Geol. 13 (2) (2023) 171–188.
[37] J. Tuduri, Processus de formation et relations spatio-temporelles des minéralisations à or et argent en contexte volcanique Précambrien (Jbel Saghro, Anti-Atlas, Maroc). Implications sur les relations déformation-magmatisme-volcanisme-hydrothermalisme, Université d'Orléans, 2005.
[38] Y. Hejja, et al., Fractures distribution and basement-cover interaction in a polytectonic domain: a case study from the Saghro Massif (Eastern Anti-Atlas, Morocco), J. Afr. Earth Sci. 162 (2020), 103694.
[39] B. Baidada, et al., Geochemistry and Sm–Nd isotopic composition of the Imiter Pan-African granitoids (Saghro massif, eastern Anti-Atlas, Morocco): geotectonic implications, J. Afr. Earth Sci. 127 (2017) 99–112.
[40] A. Schiavo, et al., Notice explicative. Carte Géologique du Maroc au 1/50.000, feuille d'Imiter, Notes Mém Serv Géol Maroc 518 (2007) 1–96.
[41] M.H. Nasab, A. Agah, Mapping hydrothermal alteration zones associated with copper mineralization using ASTER data: a case study from the mirjaveh area, southeast Iran, Trans. A Basics 36 (4) (2023) 720.
[42] Y. Ninomiya, B. Fu, T.J. Cudahy, Detecting lithology with advanced spaceborne thermal emission and reflection radiometer (ASTER) multispectral thermal infrared 'radiance-at-sensor' data, Remote Sens. Environ. 99 (1–2) (2005) 127–139.
[43] P.S. Chavez Jr., An improved dark-object subtraction technique for atmospheric scattering correction of multispectral data, Remote Sens. Environ. 24 (3) (1988) 459–479.
[44] R. Amer, T. Kusky, A. El Mezayen, Remote sensing detection of gold related alteration zones in Um Rus area, Central Eastern Desert of Egypt, Adv. Space Res. 49 (1) (2012) 121–134.
[45] R.F. Kokaly, et al., Usgs Spectral Library Version 7 Data: Us Geological Survey Data Release, vol. 61, United States Geol. Surv., Reston, VA, USA, 2017.
[46] A. Shebl, M. Abdellatif, M. Badawi, M. Dawoud, A.S. Fahil, Á. Csámer, Towards better delineation of hydrothermal alterations via multi-sensor remote sensing and airborne geophysical data, Sci. Rep. 13 (1) (2023) 7406.
[47] H. Moradpour, et al., Landsat-7 and ASTER remote sensing satellite imagery for identification of iron skarn mineralization in metamorphic regions, Geocarto Int. 37 (7) (2022) 1971–1998.
[48] R. Rajan Girija, S. Mayappan, Mapping of mineral resources and lithological units: a review of remote sensing techniques, Int. J. Image Data Fusion 10 (2) (2019) 79–106.
[49] S. Gabr, A. Ghulam, T. Kusky, Detecting areas of high-potential gold mineralization using ASTER data, Ore Geol. Rev. 38 (1–2) (2010) 59–69.
[50] S. Ousmanou, E.M. Fozing, M. Kwékam, Y. Fodoue, L.D.A. Jeatsa, Application of remote sensing techniques in lithological and mineral exploration: discrimination of granitoids bearing iron and corundum deposits in southeastern Banyo, Adamawa region-Cameroon, Earth Sci. Informatics (2023) 1–27.
[51] W. Ge, Q. Cheng, L. Jing, C. Armenakis, H. Ding, Lithological discrimination using ASTER and Sentinel-2A in the Shibanjing ophiolite complex of Beishan orogenic in Inner Mongolia, China, Adv. Space Res. 62 (7) (2018) 1702–1716.
[52] Z. Ourhzif, A. Algouti, F. Hadach, Lithological mapping using landsat 8 oli and aster multispectral data in imini-ounilla district south high atlas of marrakech, Int. Arch. Photogram. Rem. Sens. Spatial Inf. Sci. 42 (2019) 1255–1262.
[53] M.Z. Khedr, et al., Remote sensing and geochemical investigations of sulfide-bearing metavolcanic and gabbroic rocks (Egypt): constraints on host-rock petrogenesis and sulfide genesis, Gondwana Res. 119 (2023) 282–312, https://doi.org/10.1016/j.gr.2023.03.021.
[54] M. Abrams, S.J. Hook, Simulated ASTER data for geologic studies, IEEE Trans. Geosci. Rem. Sens. 33 (3) (1995) 692–699.
[55] I. Serbouti, et al., Improved lithological map of large complex semi-arid regions using spectral and textural datasets within google earth engine and fused machine learning multi-classifiers, Rem. Sens. 14 (21) (2022) 5498.
[56] A.B. Pour, M. Hashim, J.K. Hong, Y. Park, Lithological and alteration mineral mapping in poorly exposed lithologies using Landsat-8 and ASTER satellite data: north-eastern Graham Land, Antarctic Peninsula, Ore Geol. Rev. 108 (2019) 112–133.
[57] A. Villa, J.A. Benediktsson, J. Chanussot, C. Jutten, Hyperspectral image classification with independent component discriminant analysis, IEEE Trans. Geosci. Rem. Sens. 49 (12) (2011) 4865–4876.
[58] A. Hyvärinen, E. Oja, Independent component analysis: algorithms and applications, Neural Network. 13 (4–5) (2000) 411–430.
[59] C. Kumar, A. Shetty, S. Raval, R. Sharma, P.K.C. Ray, Lithological discrimination and mapping using ASTER SWIR Data in the Udaipur area of Rajasthan, India, Procedia Earth Planet. Sci. 11 (2015) 180–188.
[60] L. Xu, et al., Palaeoenvironmental evolution based on elemental geochemistry of the wufeng-longmaxi shales in western hubei, middle yangtze, China, Minerals 13 (4) (2023) 502.
[61] S. Gates-Rector, T. Blanton, The powder diffraction file: a quality materials characterization database, Powder Diffr. 34 (4) (2019) 352–360.
[62] T. Degen, M. Sadki, E. Bron, U. König, G. Nénert, The highscore suite, Powder Diffr. 29 (S2) (2014) S13–S18.
[63] A. Altomare, C. Cuocci, C. Giacovazzo, A. Moliterni, R. Rizzi, QUALX: a computer program for qualitative analysis using powder diffraction data, J. Appl. Crystallogr. 41 (4) (2008) 815–817.
[64] A. Altomare, N. Corriero, C. Cuocci, A. Falcicchio, A. Moliterni, R. Rizzi, QUALX2. 0: a qualitative phase analysis software using the freely available database POW_COD, J. Appl. Crystallogr. 48 (2) (2015) 598–603.
[65] M. Bortolotti, L. Lutterotti, I. Lonardelli, ReX: a computer program for structural analysis using powder diffraction data, J. Appl. Crystallogr. 42 (3) (2009) 538–539.

[66] A. Emam, Z. Hamimi, A. El-Fakharani, E. Abdel-Rahman, J.G. Barreiro, M.Y. Abo-Soliman, Utilization of ASTER and OLI data for lithological mapping of nugrus-hafafit area, south eastern desert of Egypt, Arabian J. Geosci. 11 (2018) 1–22.
[67] M.F. Sadek, M.W. Ali-Bik, S.M. Hassan, Late Neoproterozoic basement rocks of Kadabora-Suwayqat area, Central Eastern Desert, Egypt: geochemical and remote sensing characterization, Arabian J. Geosci. 8 (2015) 10459–10479.
[68] A.M. Mahdi, A.M. Eldosouky, S.O. El Khateeb, A.M. Youssef, A.A. Saad, Integration of remote sensing and geophysical data for the extraction of hydrothermal alteration zones and lineaments; Gabal Shilman basement area, Southeastern Desert, Egypt, J. Afr. Earth Sci. 194 (2022), 104640.
[69] S.M.A. Khashaba, N.H. El-Shibiny, S.M. Hassan, E. Takazawa, M.Z. Khedr, Application of remote sensing data integration in detecting mineralized granitic zones: a case study of the Gabal Al-Ijlah Al-Hamra, Central Eastern Desert, Egypt, J. Afr. Earth Sci. 200 (2023), 104855.
[70] H.A. Inoh, A. Rajji, M. Eddardouri, M. Tayebi, Structural and mineral mapping using multispectral images in the Central High Atlas of Morocco, Estud. Geol. (Madr.) 79 (1) (2023) e148.
[71] M. Safari, A. Maghsoudi, A.B. Pour, Application of Landsat-8 and ASTER satellite remote sensing data for porphyry copper exploration: a case study from Shahr-e-Babak, Kerman, south of Iran, Geocarto Int. 33 (11) (2018) 1186–1201.
[72] S. Rajendran, S. Nasir, ASTER capability in mapping of mineral resources of arid region: a review on mapping of mineral resources of the Sultanate of Oman, Ore Geol. Rev. 108 (2019) 33–53.
[73] J.D.T. Wambo, et al., Identifying high potential zones of gold mineralization in a sub-tropical region using Landsat-8 and ASTER remote sensing data: a case study of the Ngoura-Colomines goldfield, eastern Cameroon, Ore Geol. Rev. 122 (2020), 103530.
[74] M.A. El Zalaky, M.E. Essam, R.A. El Arefy, Assessment of band ratios and feature-oriented principal component selection (FPCS) techniques for iron oxides mapping with relation to radioactivity using landsat 8 at Bahariya Oasis, Egypt. Res 10 (10) (2018).
[75] M. Sekandari, et al., Application of landsat-8, sentinel-2, ASTER and WorldView-3 spectral imagery for exploration of carbonate-hosted Pb-Zn deposits in the central Iranian terrane (CIT), Rem. Sens. 12 (8) (2020) 1239.
[76] D.F. Ducart, A.M. Silva, C.L.B. Toledo, L.M. de Assis, Mapping iron oxides with landsat-8/OLI and EO-1/hyperion imagery from the serra norte iron deposits in the carajás mineral province, Brazil, Brazilian J. Geol. 46 (2016) 331–349.
[77] ASD TerraSpec Halo | Handheld Mineral Identifier | Product support | Malvern Panalytical." https://www.malvernpanalytical.com/en/support/product-support/asd-range/terraspec-range/terraspec-halo-mineral-identifier (accessed May 04, 2023).
[78] R. Chalkley, R.A. Crane, M. Eyre, K. Hicks, K.-M. Jackson, K.A. Hudson-Edwards, A multi-scale feasibility study into acid mine drainage (AMD) monitoring using same-day observations, Rem. Sens. 15 (1) (2023) 76.
[79] E.E. Maras, M. Caniberk, M.S. Odabas, B. Degerli, S.S. Maras, H.H. Maras, An evaluation of the relationship between physical/mechanical properties and mineralogy of landscape rocks as determined by hyperspectral reflectance, Arabian J. Geosci. 9 (2016) 1–10.
[80] TerraSpec Halo User Manual | Malvern Panalytical." https://www.malvernpanalytical.com/fr/learn/knowledge-center/user-manuals/terraspec-halo-user-manual (accessed May 04, 2023).
[81] P. Fleischmann, Using Infrared Spectroscopy to Assess Paleofluid Flow Characteristics of Clay Gouge of the Moab Fault, UT, 2022.
[82] C. Madubuike, T. Brikowski, A. Moulding, Using infrared spectrometry to deduc e fluid history from an exploration core, Emigrant Peak Geothermal Prospect, Northern Fish Lake Valley, Nevada, USA, Trans. Resour. s Counc. (2016) 445–454.
[83] M.W. Ali-Bik, M.F. Sadek, S.M. Hassan, Basement rocks around the eastern sector of Baranis-Aswan road, Egypt: remote sensing data analysis and petrology, Egypt. J. Remote Sens. Sp. Sci. 25 (1) (2022) 113–124.
[84] V. Shankar, Field characterization by Near Infrared (NIR) mineral identifiers-A new prospecting approach, Procedia earth Planet. Sci. 11 (2015) 198–203.
[85] J. Cloutier, S.J. Piercey, J. Huntington, Mineralogy, mineral chemistry and SWIR spectral reflectance of chlorite and white mica, Minerals 11 (5) (2021) 471.
[86] R.N. Clark, A.N. Rencz, Spectroscopy of rocks and minerals, and principles of spectroscopy, Man. Remote Sens 3 (11) (1999) 3–58.
[87] Y. Morsli, Y. Zerhouni, S. Maimouni, S. Alikouss, H. Kadir, Z. Baroudi, Pegmatite mapping using spectroradiometry and ASTER data (Zenaga, Central Anti-Atlas, Morocco), J. Afr. Earth Sci. 177 (2021), 104153.